Ultrasound-Driven Programmable Artificial Muscles

Zhan Shi†, Zhiyuan Zhang†, Daniel Ahmed*

Affiliations:

Acoustic Robotics Systems Laboratory, Institute of Robotics and Intelligent Systems, Department of Mechanical and Process Engineering, ETH Zurich, CH-8803 Zurich, Switzerland

*Corresponding author. Email: dahmed@ethz.ch

†These authors contribute equally to this work.

ABSTRACT

Despite their promise for technological and medical innovations, the advancement of artificial muscles faces challenges in dynamic programmability, wireless control, scalability, and responsiveness. Ultrasound offers a promising yet underutilized solution, providing effective and robust actuation. We introduce an innovative design paradigm for soft artificial muscles, utilizing tens of thousands of resonant microbubbles for targeted activation, enabling a wide range of programmable motions. We developed a comprehensive theoretical model and conducted various applications: from actuating soft grippers and powering centimeter-scale biomimetic stingraybots for propulsion to demonstrating the multimodal shape transformation of a functional surface and equipping static objects with transformative robotic skins for mobility. Our approach is marked by its compactness, high force intensity, rapid responsiveness, and lightweightness. The customizable, scalable design of our artificial muscles offers both immediate and long-term impact on robotics, wearable technology, haptics, prosthetic development, and the development of avant-garde biomedical devices like soft surgical tools.

One-Sentence Summary: We introduced a first-of-its-kind, programmable artificial muscle using ultrasound-activated microbubbles, providing a compact, responsive, and scalable solution.

INTRODUCTION

Flexible, compact, and adaptive artificial muscles (*1,2*), are set to be transformative across multiple fields, including soft robotics (*3,4*), wearables for human-machine interactions and healthcare, like prosthetics (*5,6*), orthotics (*7,8*), and embodied sensing (*9,10*), and assistance in sophisticated manufacturing through dexterous manipulation (*11,12*). In addition, they can also become pivotal in the development of advanced biomedical devices, such as soft surgical tools (*13,14*), artificial heart (*15,16*), and implantable electrodes (*17,18*). Despite their potential, current artificial muscles like tendon-based (*19,20*) and pneumatic types (*21,22*) encounter substantial challenges in wireless control, integration, and miniaturization due to dependencies on tethering, complex operational mechanisms, and large input requirements. While external stimuli such as chemicals (*23,24*), light (*25,26*), temperature (*27,28*), electronic fields (*29–31*), and magnetic fields (*32–35*) have been deployed for wireless actuation, they typically fall short in scalability and responsiveness, with only a select few capable of targeted actuation, often requiring intricate material pre-programming. Therefore, creating an artificial muscle that is both responsive and versatile, as well as wireless, lightweight, programmable, scalable, and compatible still remains to be a formidable challenge.

Acoustic actuation emerges as a promising solution, offering powerful and simplified actuation sources, multi-mode programming, wireless operation, and ultrafast, reversible responses within milliseconds for micromachines (*36–46*). Yet, research into ultrasound-based artificial muscles has been surprisingly limited, primarily due to the weak acoustic forces they produce. This limitation becomes more pronounced with larger muscles, which necessitate lower frequencies to synchronize with their increased dimensions. Furthermore, the typically low acoustic contrast factors of soft materials, especially when immersed in water, lead to inadequate force generation for efficient functionality. This predicament is exacerbated by a lack of understanding of the interactions between acoustics and soft materials, impeding the progress of effective acoustic-driven muscle systems.

We introduce a fundamentally new artificial muscle built on acoustically activated microbubble-array. Microbubbles, resonant by character, are highly effective at focusing acoustic energy, thus allowing a weak sound source to significantly amplify its response. This synthetic muscle includes a thin, transparent, and flexible beam that houses over 80,000 microcavities arranged in discrete arrays, each designed to confine microbubbles of various sizes. When these microbubbles are acoustically stimulated, they produce thrust, causing the beam to deform. Tailored activation of differently sized microbubble-arrays through programmable sweep-frequency ultrasound excitation results in uniformly distributed point forces, allowing multi-modal deformation. These synthetic muscles showcase remarkable features: dense compactness of 3,000 microbubbles per square millimeter, lightweight at 0.058 mg/mm², the ability to exert a significant force of 180 μN/mm², a rapid response of 20 milliseconds, and a broader range of motions. A theoretical model has been developed to describe the ultrasound actuation mechanism at play. Demonstrating their adaptability, these muscles can actuate soft grippers capable of handling objects dozens of times their own body weight, power centimeter-scale biomimetic stingraybots for propulsion, deliver multimodal shape transformation, and apply a robotic skin to animate stationary objects. The tunable nature and scalability of these microbubble-arrays herald a new era of possibilities, positioning these acoustic artificial muscles at the forefront of innovation in robotics, wearable technology, prosthetic development, and soft surgical devices.

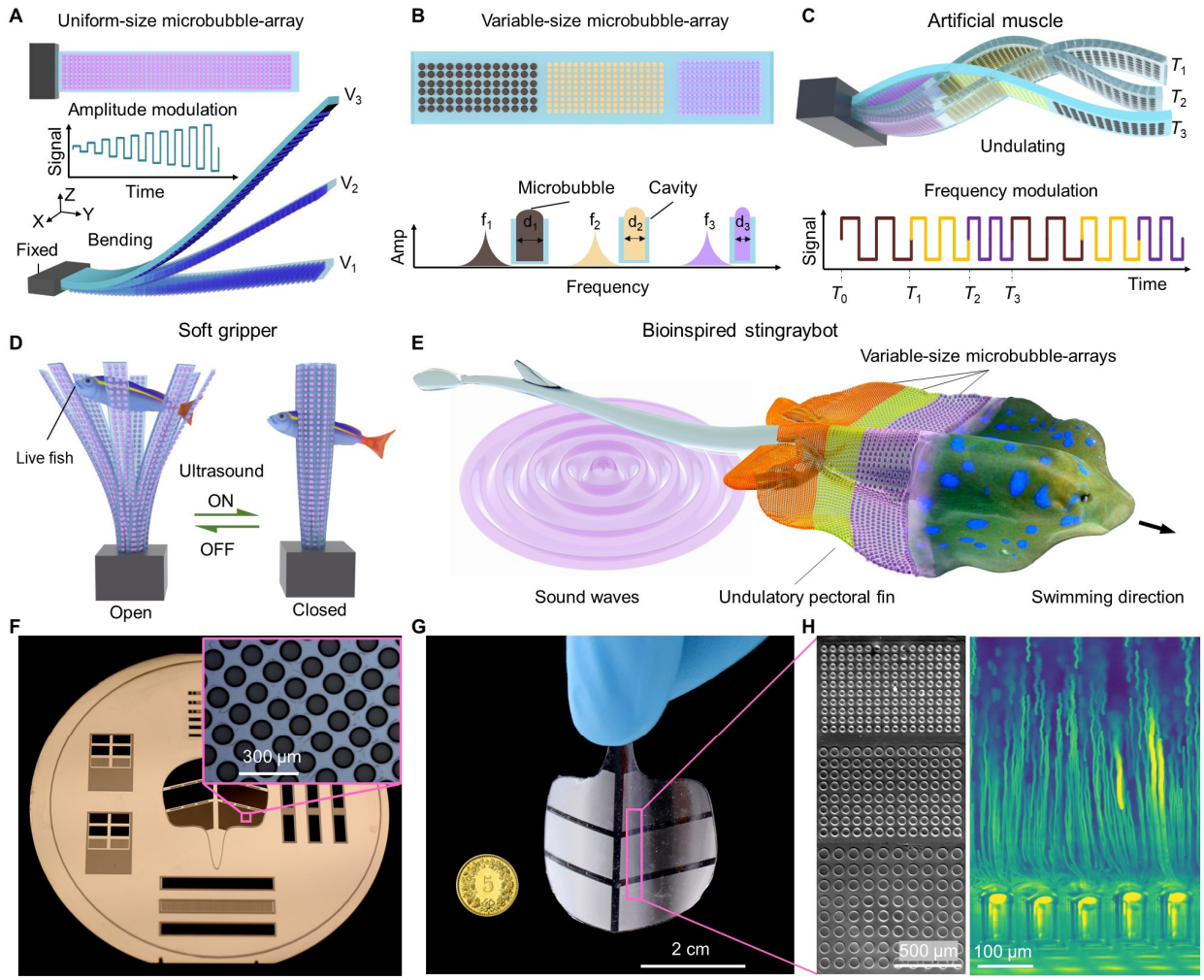

Fig. 1. Ultrasound-actuated Microbubble-array artificial muscles. (**A**) A uniform-size microbubble-array artificial muscle consists of tens of thousands of microbubbles on its bottom surface. Under continuous high-frequency ultrasound excitation, the artificial muscle bends upwards with different excitation voltages, labeled as V_1, V_2, and V_3. The inset shows the input ultrasound signal with modulated amplitude versus time. (**B**) A variable-size microbubble-array artificial muscle consists of three microbubble-arrays with different microbubble diameters featuring different natural frequencies represented by distinct colors. (**C**) Under sweeping-frequency ultrasound excitation, the artificial muscle exhibits multi-mode deformation in the time domain, shown at time points T_1, T_2, and T_3. (**D**) Schematic of a soft gripper constructed with an array of tentacles which patterned with uniform-size microbubble-arrays. Upon ultrasound excitation, the tentacles close simultaneously in milliseconds. (**E**) Schematic of a bioinspired stingraybot incorporates variable-size microbubble-arrays. Under sweeping-frequency ultrasound excitation, the stingraybot enacts undulating propulsion. (**F**) A silicon wafer with micropillar arrays serve as the negative mold of microbubble cavities in standard soft-lithography fabrication. Inset shows the micropillar array. **(G)** A prototype of the stingraybot. Inset shows a 5-cent Swiss franc coin. (**H**) Left: Trapped microbubbles on the stingraybot. Right: Upward jetting microstreaming generated from a microbubble-array oscillating under ultrasound excitation demonstrated by 6 μm diameter tracer microparticles.

RESULTS

Design and fabrication of microbubble-array artificial muscles

The ultrasound-driven artificial muscle features a thin, flexible rectangular beam with microbubbles arrays on one side. In the initial design, depicted in **Fig. 1A**, we incorporated microcavities of uniform size on the bottom surface of the muscle. When the muscle was submerged in an acoustic chamber filled with water, it resulted in the simultaneous capture of tens of thousands of gas-filled microbubbles within the cavities, a phenomenon driven by surface tension. We then anchored one end of the muscle while leaving the other free to act as a cantilever. Subsequently, we activated a piezoelectric transducer to generate an external ultrasound. The incident sound waves, passing through the liquid, induce microbubble oscillations, generating acoustic streaming and radiation forces. As all microbubbles in the muscle were of the same size, synchronous oscillation was observed. This collective oscillation in turn exerted a uniformly opposing force on the bottom surface of the muscle, causing it to flex upwards. Modulating the ultrasound excitation voltage resulted in differing deformation amplitude of the synthetic muscle.

We then designed an artificial muscle that incorporates microbubble-arrays of varying sizes, illustrated in **Fig. 1B**. Microbubbles of different sizes have distinct natural frequencies and hence can be selectively excited, generating a local opposing force and selective deformation of the synthetic muscle. By applying a sweeping ultrasound signal that encompasses the natural frequencies of all microbubbles, we sequentially activated the different arrays along the long axis of the muscle. This resulted in intricate undulatory motions over multiple excitation cycles (**Fig. 1C**). Thus, in implementing this arrangement of microbubbles of varied sizes and their selective excitation through ultrasound modulation, we have unlocked a new capability to control multi-mode deformations. The adaptability and versatility of these artificial muscles facilitate a wide array of applications. For instances, we have employed these artificial muscles in the development of a soft gripper, crafted to delicately handle live fish (**Fig. 1D**), as well as in the design of a soft swimmer, inspired by the form and function of stingrays (**Fig. 1E**).

Prototypes of these artificial muscles were fabricated using a high-resolution mold-replica method (*47*). Initially, we patterned micropillar arrays on a silicon wafer using standard soft lithography as negative molds for the cylindrical microcavities (**Fig. 1F**). All pillars were designed of identical heights and spacings, corresponding to dimensions of desired microbubbles (**Fig. S1**). We then spin coated a thin layer of polydimethylsiloxane (PDMS) onto the wafer, with heights ranging from 80 to 250 μm (**Fig. S2**). After curing, we cropped and stripped these artificial muscles, including the artificial stingray, depicted in **Fig. 1G**. Further details of our fabrication process can be found in the Materials and Methods section. **Fig. 1H** shows the microbubbles trapped on the stringraybot and the upward microstreaming jetting produced under ultrasound excitation.

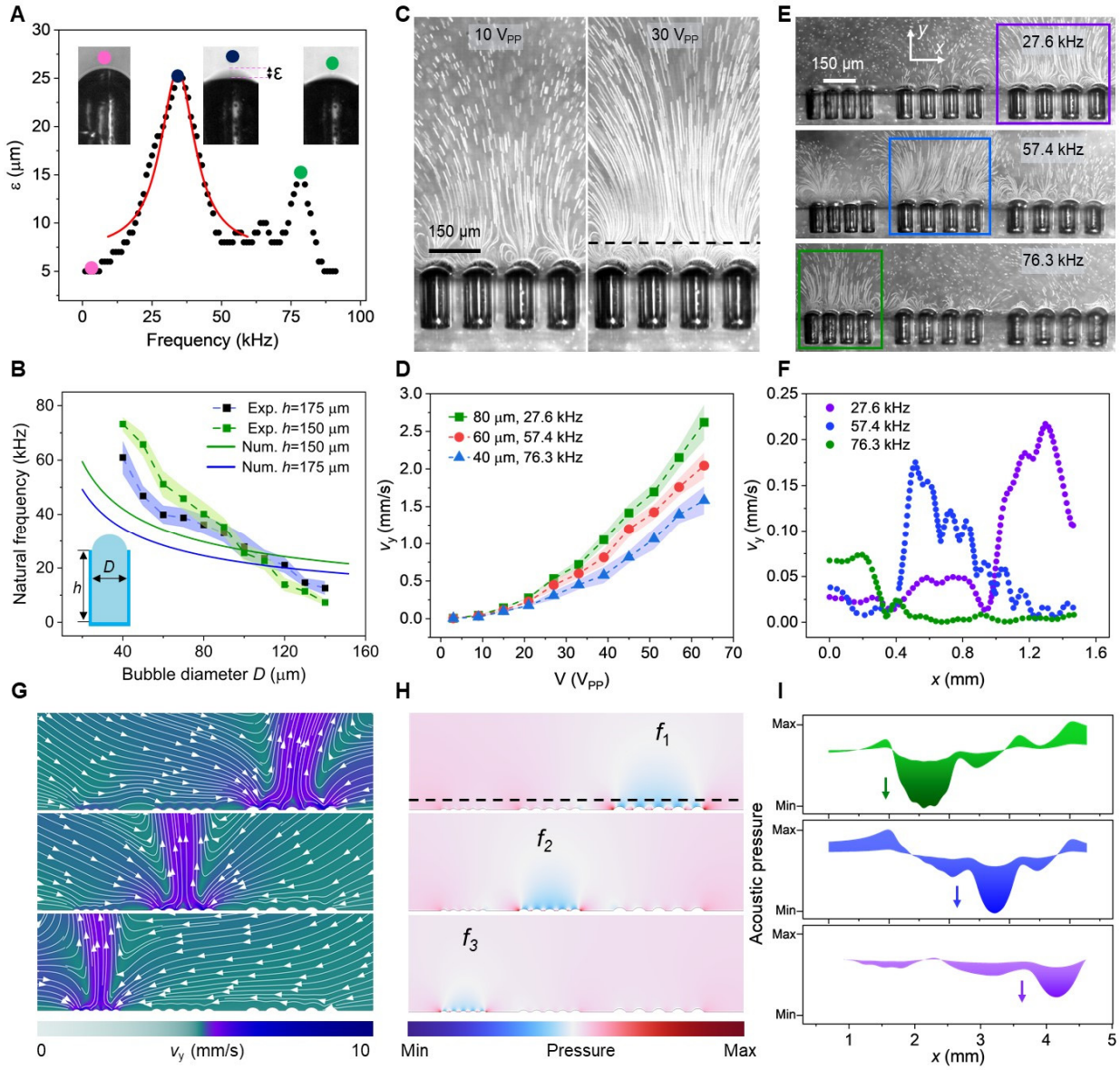

Fig. 2. Characterization of microbubble-arrays. (**A**) Plot of the oscillation amplitude of a 60 × 150 μm microbubble versus different ultrasound excitation frequencies. The resonance frequency is 35.5 kHz. (**B**) Plot of the natural frequencies of microbubbles with diameters ranging from 40 to 140 μm. Two different lengths (h) of bubbles are respectively tested, 150 μm (green) and 175 μm (blue). (**C**) Microstreaming generated by a 4×4 80×150 μm microbubble-array under the excitation frequency of 27.6 kHz and two different voltages of 10 V_{PP} (left panel) and 30 V_{PP} (right panel). The black dotted line denotes the measure position of the microstreaming velocity, which is 80 μm away from the surface. (**D**) Plot of microstreaming velocity versus ultrasound excitation voltage respectively measured by 4×4 microbubble-arrays with three different sizes (40, 60, and 80 μm) × 150 μm. (**E**) Microstreaming respectively generated by (40, 60, and 80 μm) × 150 μm microbubble-arrays under ultrasound frequencies of 27.6 kHz (purple), 57.4 kHz (blue) and 76.3 kHz (green). Colored boxes indicate the activated microbubbles. (**F**) Plot of microstreaming velocity along the long axis of the variable-size microbubble-array in (**E**) under different excitation frequencies. Simulations of (**G**) microstreaming and (**H**) acoustic pressure. (**I**)

Plot of acoustic pressure under different excitation voltages ranging from 10 to 60 V_{PP}. Arrows represent the increase of input strength.

Characterization of microbubble-arrays

To further our understanding and control of microbubble-arrays in artificial muscles, we examined the interaction between microbubble-arrays and ultrasound signals. Our experimental setup included a transducer bonded onto a glass slide, positioned adjacent to a water-filled chamber (10×10×5 mm). The synthetic muscle was placed in the center of the chamber with one end clamped to the sidewall and other end left free (**Fig. S3**), and the entire setup was mounted on an inverted microscope. Using a high-speed camera, we observed the transient dynamics of the microbubble while applying acoustic fields with excitation frequencies of 10−100 kHz and voltage amplitudes of 10−60 V_{PP}. Further details on the acoustic setup are provided in the Materials and Methods section.

We began by identifying the natural frequency of uniformly sized 4×4 microbubbles confined within cavities. For example, a microbubble measuring 60×150 μm (diameter × length) exhibited its largest oscillation amplitude at an excitation frequency of 35.5 kHz (**Fig. 2A**). We then measured the natural frequencies of microbubble-arrays with diameters from 40 to 140 μm, while maintaining a constant excitation voltage of 15 V_{PP}. The results, shown in **Fig. 2B**, revealed that both microbubbles of lengths 150 μm (green line) and 175 μm (blue line) exhibited a decreasing natural frequency as the bubble diameter increased. This is expected as the natural frequency of the microbubbles scales inversely with their diameter (*48*). The discrepancy between numerical calculations and experimental results could be attributed to acoustic coupling among microbubbles (see Supplementary Text). Distinguishable natural frequencies among differently sized microbubbles facilitate selective ultrasound excitation, enabling the creation of programmable microbubble-arrays.

We then evaluated the jetting microstreaming produced by microbubble-arrays at different excitation voltages. Three artificial muscles, each composed of uniformly sized 4×4 microbubbles of 150 μm in length but differing diameters (40 μm, 60 μm, and 80 μm), were tested individually (**Fig. 2C** and **Movie S1**). When activated at their respective natural frequencies—38.7 kHz, 52.5 kHz, and 68.4 kHz—we noted that the average microstreaming velocity scaled quadratically with voltage (**Fig. 2D**). A stronger microstreaming indicates that the reverse thrust developed by the microbubble-array is larger, which can be modulated through varying excitation voltage and bubble size. We further investigated the selective actuation of variable-sized microbubble-arrays within an artificial muscle, as microscopically demonstrated in **Fig. 2E**. Particle image velocimetry (PIV) analysis, as shown in **Fig. 2F** and **Fig. S4**, reveals that the microstreaming developed by the 80 μm microbubble-array was markedly stronger compared to the other two microbubble-arrays, with an average velocity of 0.23 mm/s at 27.6 kHz and 60 V_{PP}. Although the microstreaming velocity around the other bubble arrays was not negligible, it was markedly lower, at less than 0.05 mm/s. When the frequency is adjusted to 57.4 kHz, the 60 μm microbubble-array is selectively activated, exhibiting significantly more intense streaming at 0.18 mm/s. Similarly, adjusting the frequency to 76.3 kHz selectively activates the 40 μm array, resulting in more intense streaming at 0.075 mm/s, in contrast to other arrays. The simulation results of the microstreaming (**Fig. 2G**) and the acoustic pressure field (**Fig. 2H**) are consistent with these experimental findings. **Fig. 2I** shows as increasing the input strength, the acoustic pressure difference between active and quiescent microbubble-arrays is always distinguishable. Furthermore, when sweeping the ultrasound frequency from 10 to 90 kHz over a 4-second period at 30 V_{PP}, a sequential propagation

of the excitation wave through the microbubble-arrays was observed (**Movie S1**). This suggests that acoustic coupling is not significant enough to impede selectivity, thereby supporting the potential for programmable sweeping-frequency ultrasound excitation within microbubble-arrays.

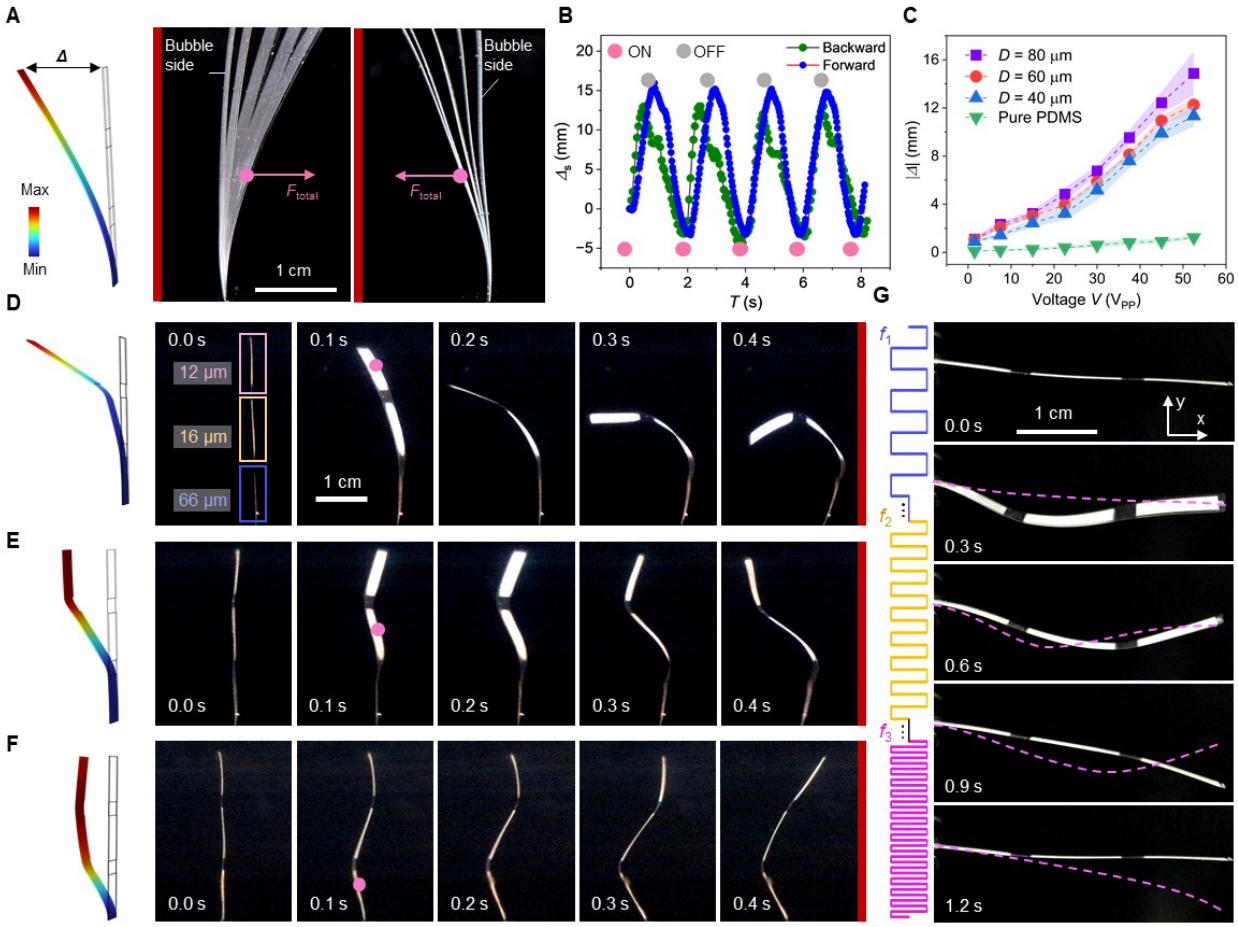

Fig. 3. Actuation of microbubble-array artificial muscles. (**A**) Simulation and time lapse figures of a uniform-size microbubble-array artificial muscle with microbubbles respectively positioned at left-side and right-side of the artificial muscle. The magenta arrow shows the resultant force acting on the muscle. The red line denotes the location of the transducer. The color bar of the simulation denotes the bending amplitude. (**B**) Plot of the bending amplitude of the muscle tip over multiple excitation cycles with an average repeat positioning error of ±0.8 mm. (**C**) Bending amplitude of uniform-sized artificial muscles with diameters of 40 μm, 60 μm, and 80 μm microbubble-arrays and without microbubbles under excitation voltages from 1.5 to 52.5 V_{PP}. The microbubbles have a constant length of 50 μm. All the muscles bent in the direction as shown in the left panel of (A). (**D** to **F**) Simulations and time lapse images of the individual deformation shapes of a variable-size microbubble-array artificial muscle with diameters of 12 μm, 16 μm, and 66 μm microbubble-arrays. The microbubbles have a constant length of 50 μm. (**G**) Time lapse images of the variable-size artificial muscle under sweeping-frequency ultrasound excitation with frequencies ranging from 20 to 90 kHz. The ultrasound excitation voltage from panel **D** to **G** was consistently at 60 V_{PP}. The artificial muscles utilized here are all measuring 3 cm in length, 0.5 cm in width, and 80 μm in thickness.

Actuation of microbubble-array artificial muscles

The versatility of microbubble-arrays in terms of scalability, programmability, and selectivity enables an innovative approach for designing soft actuators with enhanced flexibility and control. We characterize this in an experimental setup, depicted in **Fig. S5**, which comprises a rectangular tank of deionized water, with transducers mounted to its inner walls. A high-sensitivity camera was used to capture the deformation dynamics of the artificial muscles. Further details on the acoustic setup are provided in the Materials and Methods section.

To determine the key factors influencing muscle deformation, a set of control experiments were performed. These experiments revealed that, in the absence of microbubbles, the synthetic muscles exhibited minimum deformation, with no noticeable jetting microstreaming observable across excitation frequencies from 1 to 100 kHz at 60 V_{PP} (**Movie S1**). We then tested the bending deformation of uniformly sized microbubble-array muscles with 3 cm in length, 0.5 cm in width, and 80 μm in thickness, patterned with 10,000 microbubble cavities (each 40 μm in diameter and 50 μm long). Upon ultrasound stimulation at 9.5 kHz and 60 V_{PP}, we noted pronounced microstreaming, resulting in substantial deformation in the synthetic muscle (**Movie S1**). Subsequent experiments involved adjusting the transducer's position relative to the microbubble-embedded side of the muscle. The transducer was positioned in four distinct orientations: close to and distant from the microbubble-embedded side, as well as perpendicularly aligned with both the right and left sides relative to the microbubble-array (**Fig. 3A**, **Fig. S6**, and **Movie S2**). When acoustically activated with a constant excitation amplitude of 60 V_{PP}, the muscle demonstrated a consistent bending direction regardless of these positions i.e., all samples bent in the direction opposite to the microbubble-array side, despite the variations in bending amplitudes measured of 15.4 mm, 6.68 mm, 7.27 mm, and 5.90 mm. This indicates that the reverse thrust generated by the microbubble-arrays is the predominant force driving behind muscle deformation. Insets in **Fig. 3A** depict the direction of the resultant force acting on the muscle. Our simulation that applies a uniform load reflects the deformation seen in our experiments, thereby validating our force analysis. When stimulated with ultrasound pulses, the uniform-sized muscle exhibited repeatable bending cycles, with an error of ±0.8 mm, representing 2.7% of the total beam length (**Fig. 3B**). Additionally, **Fig. 3C** illustrates the mean bending amplitude of our synthetic muscles patterned with differently size microbubbles (diameters of 40 μm, 60 μm, and 80 μm) scales quadratically with voltages; and under identical voltage, larger microbubbles exert a more substantial bending amplitude.

We further investigated the deformation of an artificial muscle equipped with variable-size microbubble-arrays. This muscle, with the dimensions of 3 cm in length, 0.5 cm in width, and 80 μm in thickness, consists of three discretized arrays of microbubble with dimensions: 12 μm × 50 μm, 16 μm × 50 μm, and 66 μm × 50 μm. Upon stimulation at its natural frequency, the 12 μm × 50 μm microbubble-array, covering an area of 0.5 cm^2, induced a downward deformation in the corresponding muscle region, as depicted in **Fig. 3D** to **3F** and **Movie S3**. This deformation pattern aligns with simulations, where only the top region of the artificial muscle was subjected to a uniform load. Similarly, when the frequency was increased to match the natural frequencies of the 16 μm and 66 μm bubble arrays, respectively, the muscle showed a localized downward deformation in this new region, while the area stimulated previously reverted to its original state. We demonstrated an undulatory sinusoidal deformation pattern by actuating the artificial muscle with a sweeping-frequency ultrasound excitation ranging from 30 to 90 kHz. This continuous, time-dependent motion, as shown in **Fig. 3G** and **Movie S3**, resulted from the periodic reverse

thrust generated across different regions of the muscle. For each deformation, the excitation cycle was repeated more than ten times, and the average repeat positioning error of the muscle tip was ± 0.4 mm.

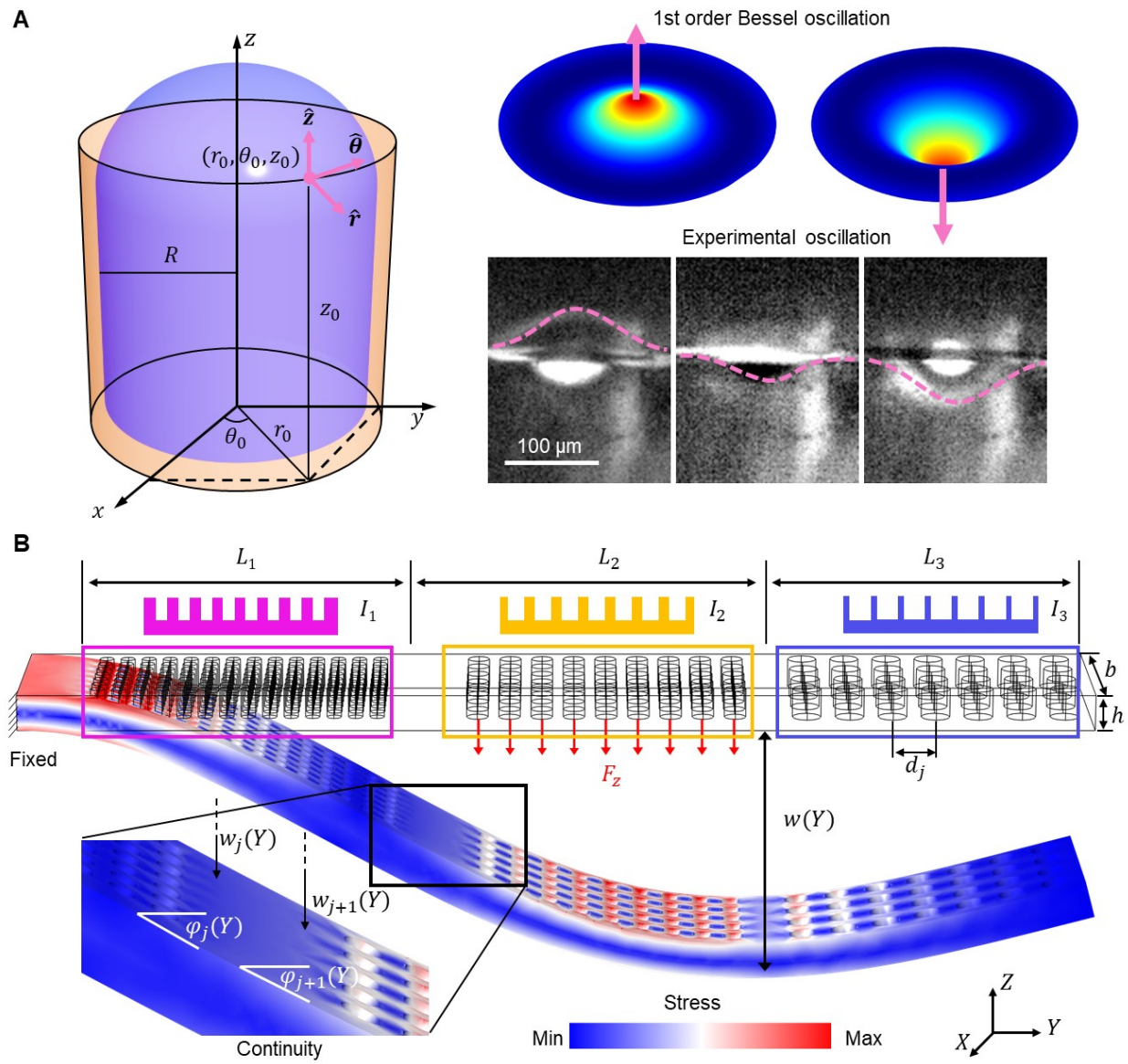

Fig. 4. Illustration of theoretical modeling of a single microbubble and the entire artificial muscle. (A) An axisymmetric cylinder microbubble characterized with cylindrical coordinates with the theoretical Bessel oscillation and recorded experimental oscillation. **(B)** Modelling and simulation of the variable-size microbubbles arrays artificial muscle. The purple, yellow and pink box represent the different sizes microbubble-array element, upper shows the schematic of the cross-section of the artificial muscle, which have corresponding momentum inertia I_j ($j = 1,2,3$). Inset shows the continuous deformation conditions. F_z denotes the thrust force generated by the microstreaming. $w(Y)$ and $\varphi(Y)$ denote the deflection and rotation angle along the long axis (Y axis).

Modeling of microbubble-array artificial muscles

Artificial muscles, featuring arrays of variable-size microbubbles, enable selective deformation and deliver an extensive range of motion when subjected to ultrasound at targeted frequencies. We have developed a theoretical model to further our comprehension of the response of soft artificial muscles to sound waves. This model divides the entire artificial muscle into discrete segments that correspond to the patterned microbubble-arrays, as illustrated in **Fig. 4**.

We began our analysis by examining the acoustic radiation force acting on a single trapped microbubble based on the cylindrical coordinates (**Fig. 4A**). The experimental recording captured a microbubble oscillation in shapes closely matching the solution of the 1st Bessel function $J_1(k_0 r)$, where $k_0 = \omega / c_0$, with ω denoting the oscillation frequency and c_0 representing the speed of sound (**Fig. 4A**). Due to *z*-axis symmetry of the microbubble, the net outward radiating force F_z along the central axis is

$$F_z = \left(\oint_{\boldsymbol{A}} \boldsymbol{S}_T \cdot \mathrm{d}\boldsymbol{A} \right) \cdot \hat{\boldsymbol{e}}_{\boldsymbol{z}} \tag{1}$$

where $\boldsymbol{S}_T$ is the Brillouin stress tensor, and $\boldsymbol{A}$ is the area of the bubble interface (*49*). We postulate that the force acting on each microbubble can be represented as a point force, acting perpendicular to the oscillation surface. Furthermore, we assumed that all microbubbles in the array are subject to homogenous force conditions. Consequently, the resulting force acting on an entire segment is considered as a uniformly distributed load, denoted by $F_{u_j} = N_j F_{z_j} / S_j$, where *j* is the *j*th segment, N_j and S_j are the number of microbubbles and the area of the segment.

Next, as depicted in **Fig. 4B**, we employ a continuous boundary condition within Euler-Bernoulli theories (*50*) to synthesize the deformation of individual segments into a linearized model for the entire muscle as

$$\Delta_{\boldsymbol{z}}(Y, t) = \sum_{j=1}^{n} \frac{F_{u_j}}{E I_j}(t) W_j(Y) \quad (j = 1,2,3) \tag{2}$$

Here, $\Delta_{\boldsymbol{z}}(Y, t)$ represents the time-varying deformation of the artificial muscle relevant at location Y along its longitudinal axis, with t denotes the ultrasound excitation time. W_j is the deflection mode of the *j*th element, E is the Young's modulus of the soft materials, and I_j is the momentum inertia for each segment.

Our model is applicable to artificial muscles featuring both uniform and variable-size microbubble-arrays. It demonstrates that the deformation amplitude of an artificial muscle can be amplified by increasing the ultrasound excitation voltage, as well as the number and size of microbubble cavities. This theory is validated by the experimental data presented in **Fig. 3C**. Furthermore, a larger deformation can also be achieved by either reducing the Young's modulus of the materials or by decreasing the beam's thickness (**Fig. S7**).

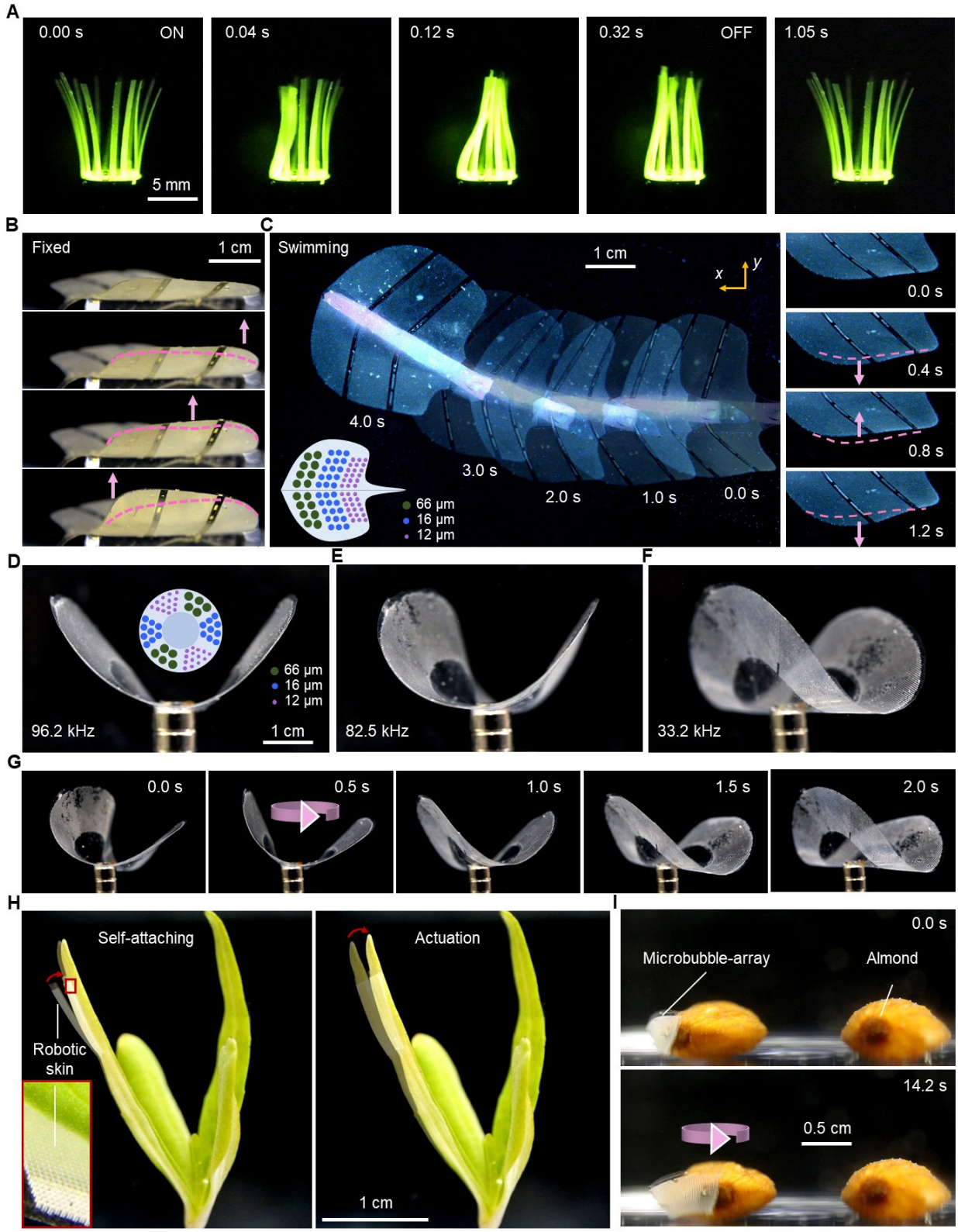

Fig. 5. Applications of microbubble-array artificial muscles. (**A**) Actuation of a soft gripper features multiple uniform-sized microbubble-array artificial muscles as tentacles. (**B**) Undulation motion of the microbubble-array fins of the bioinspired stingraybot before releasing. The magenta

dotted line and arrow respectively denote the shape of the fins in the last time lapse and the moving direction of the fins in the current time lapse. (**C**) Forward swimming of the stringraybot. Undulatory motion of the fins during swimming is shown in the right panel. Inset shows the schematic of the microbubble-array patterned on the fins. (**D to F**) Multimodal shape transformation of a circular surface under the continuous ultrasound excitation frequencies of 96.2 kHz, 82.5 kHz, and 33.2 kHz, respectively. Inset shows the schematic of the microbubble-array patterned on the surface. (**G**) Dynamic shape transformation of the circular surface under sweeping-frequency ultrasound excitation spanning from 60 kHz to 90 kHz over 2 seconds. (**H**) Closing of a piece of grass and (**I**) rotating of an almond by a conformable microbubble-array robotic skin. Inset shows the zoom-in view of the microbubble-array.

Applications of microbubble-array artificial muscles

The development of versatile microbubble-array artificial muscles presents an exciting alternative for wireless actuation and paves the way for innovative designs in the field of soft robotics. As a representation, we introduced a miniaturized soft gripper comprised of eight uniform-sized artificial muscles, which are uniformly distributed in a manner resembling the petals of a flower. Each tentacle measures 10 mm, 0.7 mm, and 0.08 mm in length, width, and thickness, respectively, and houses 60,000 microbubbles when submerged in water. In the absence of ultrasound, the flower-shaped gripper remains at rest in an open state. When subjected to a continuous acoustic excitation at 95.5 kHz and 60 V_{PP}, it swiftly closes within 20 milliseconds; when the acoustic stimulus is deactivated, it reopens (**Fig. 5A** and **Movie S4**). We tested the robustness of the gripper with multiple orientation and locations in the acoustic tank, and the gripper is able to be actuated independently on the position of the transducer (**Movie S4**). We also demonstrated three distinct grippers, each featuring tentacles with microbubble-arrays in varying diameters: 12 μm, 16 μm, and 66 μm. These grippers can be sequentially activated by sweeping the frequency range from 30 to 100 kHz, with a sweeping duration of 1.2 seconds and an applied voltage of 60 V_{PP} (**Movie S4**). Remarkably, the gripper can trap objects massing up to 250 mg, which is 35 times its own, 7 mg (**Fig. S8**). This trapping force can be bolstered by increasing the number of microbubbles within each tentacle or by adding more muscles.

We then developed a bioinspired ultrasound-controlled wireless stingraybot that features variable-size microbubble-array artificial muscles designed to resemble the fins of a natural stingray. These artificial fins are patterned with microcavity arrays of three distinct sizes from the head to tail (with the diameters of 12 μm, 16 μm, and 66 μm and height of 50 μm) on both sides of the stingraybot. When exposed to a sweeping-frequency ultrasound excitation spanning from 30 to 90 kHz over 2 seconds at 60 V_{PP}, the fins of the stingraybot exhibited an undulatory motion that mimics the movement seen in stingrays (**Fig. 5B** and **Movie S5**). Upon releasing the stingraybot, it propelled forward at an initial speed of approximately 0.8 body lengths per second (**Fig. 5C** and **Movie S5**). As a control experiment, a stingraybot without microbubbles did not exhibit undulatory motion in the fins under ultrasound excitation and it sank directly to the bottom of the acoustic tank without notable lateral displacement (**Movie S5**). The results suggest that the forward motion of the stingraybot is predominant by the propulsion force generated by the sequential undulatory motion, resulting from the reverse thrust generated by microbubble-arrays. Moreover, to steer the stingraybot, more different sizes microbubble-arrays can be patterned to enhance the selective ultrasound actuation. Additionally, we can add an external steering tail to the artificial stingray to control it swimming direction. **Fig. S9** shows a shark-tail-shaped soft robot actuating by uniform-size microbubble-array that can wiggle like a natural shark. Since the stingraybot is quiet and transparent, we envision that our stingraybot can be employed for

environmental data collection or behavioral research on real organisms, for example, detecting water quality within coral reefs and recording swarm interaction by blending into schools of fish.

We also demonstrated a multimodal shape transformer. As shown in **Fig. 5D**, the ring of functional surface with the diameter from 3 to 5 cm is patterned with six microbubble-arrays with the bubble diameters of 12 μm, 16 μm, and 66 μm and height of 50 μm. By individually applying ultrasound excitation frequencies of 96.2 kHz, 82.5 kHz, and 33.2 kHz. The surface shows selective multimodal deformation (**Fig. 5D** to **F**). Under the sweeping-frequency excitation from 60 to 90 kHz at 60 V_{PP}, the surface shows a clockwise undulatory motion (**Fig. 5G** and **Movie S6**). The surface demonstrates the remote driving capability and tuning ability of the microbubble-array artificial muscles. We envision that by patterning more sizes of microbubble-arrays and programming the ultrasound excitation frequency, the surface possesses significantly increasing modes for diverse dynamic interaction.

We finally developed the microbubble-array artificial muscle as a conformable robotic skin that can be adhered to arbitrary surfaces and empower motion to inanimate objects. In **Fig. 5H**, upon switching on the ultrasound excitation with 95.5 kHz and 60 V_{PP}, the robotic skin self-attached to the surface of a piece of grass and enabled the leaf to close (**Movie S7**). We also attached the robotic skin onto an arbitrary-shaped almond that exhibits controllable clockwise rotation as we excited it (**Fig. 5I** and **Movie S7**). The microbubble-array robotic skin offers the inanimate object diverse mobilities without notable size or mass increase. Accordingly, in the coming future, new plug-to-play microbubble-array wearable devices can be developed for human.

DISCUSSION

We have introduced a new class of soft artificial muscles that leverage acoustically activated microbubble-arrays to achieve precise and programmable actuation. These acoustic artificial muscles are characterized by their dynamic programmability, large force intensity, rapid responsiveness, wireless controllability, all while being exceptionally compact and lightweight. Our findings demonstrate that the use of resonant microbubbles allows for the amplification of acoustic energy, enabling a weak sound source to produce substantial actuation in the artificial muscle. We have successfully engineered a broad array of preprogrammed movements and applications for the artificial muscle, which are directed by the unique configuration of the microbubbles and the ultrasound excitation parameters, such as voltage and frequency. We showcased the strength and durability of these muscles by incorporating the variable-sized microbubble-arrays into devices such as a soft gripper, a biomimetic stingray robot, a shape transformer, and a robotic skin. Additionally, we devised a theoretical model that elucidates the actuation mechanism and guides the design of innovative microbubble-array patterns to enhance maneuverability. In conclusion, our microbubble-array artificial muscles offer extensive actuation maneuverability and applications in robotics, flexible electronics, wearable technologies, prosthetics, biomedical instruments, and beyond.

Despite these promising results, we recognize certain limitations. Although the microbubbles are stable for hours, the potential volumetric growth of microbubbles under continuous actuation presents a challenge. In case the microbubbles become larger, we can remove the artificial muscle from the liquid chamber and reimmerse it in the liquid, causing fresh microbubbles to become trapped. Excitingly, we have achieved preliminary promising results with

thin membrane-sealed cavity bubbles, which are exceptionally stable and have the potential to substitute for air bubbles.

Looking ahead, the potential applications of these artificial muscles span across multiple cutting-edge technologies. Future research will focus on refining the scalability of these systems, enhancing their force generation capabilities, and integrating them into complex devices for practical applications. The insights gained from this study will undoubtedly guide the next generation of soft actuation systems, driving innovation in fields that require nuanced control and delicate interaction with the surrounding environment.

SUPPLEMENTARY MATERIALS

Materials and Methods
Supplementary Text
Supplementary Figs. S1 to S9
Legends for Supplementary Movies S1 to S7

REFERENCES AND NOTES

1. Li, M., Pal, A., Aghakhani, A., Pena-Francesch, A. & Sitti, M. Soft actuators for real-world applications. *Nat. Rev. Mater.* **7**, 235–249 (2022).
2. Zhang, J. *et al.* Robotic Artificial Muscles: Current Progress and Future Perspectives. *IEEE Trans. Robot.* **35**, 761–781 (2019).
3. Laschi, C., Mazzolai, B. & Cianchetti, M. Soft robotics: Technologies and systems pushing the boundaries of robot abilities. *Sci. Robot.* **1**, eaah3690 (2016).
4. Rus, D. & Tolley, M. T. Design, fabrication and control of soft robots. *Nature* **521**, 467–475 (2015).
5. Ortiz-Catalan, M. *et al.* A highly integrated bionic hand with neural control and feedback for use in daily life. *Sci. Robot.* **8**, eadf7360 (2023).
6. Polygerinos, P., Wang, Z., Galloway, K. C., Wood, R. J. & Walsh, C. J. Soft robotic glove for combined assistance and at-home rehabilitation. *Rob. Auton. Syst.* **73**, 135–143 (2015).
7. Kang, B. B., Choi, H., Lee, H. & Cho, K. J. Exo-Glove Poly II: A Polymer-Based Soft Wearable Robot for the Hand with a Tendon-Driven Actuation System. *Soft Robot.* **6**, 214–227 (2019).
8. Zhao, H., O'Brien, K., Li, S. & Shepherd, R. F. Optoelectronically innervated soft prosthetic hand via stretchable optical waveguides. *Sci. Robot.* **1**, eaai7529 (2016).
9. Gao, W. *et al.* Fully integrated wearable sensor arrays for multiplexed in situ perspiration analysis. *Nature* **529**, 509–514 (2016).
10. Wang, C. *et al.* Monitoring of the central blood pressure waveform via a conformal ultrasonic device. *Nat. Biomed. Eng.* **2**, 687–695 (2018).
11. Abondance, S., Teeple, C. B. & Wood, R. J. A Dexterous Soft Robotic Hand for Delicate In-Hand Manipulation. *IEEE Robot. Autom. Lett.* **5**, 5502–5509 (2020).
12. Xie, Z. *et al.* Octopus-inspired sensorized soft arm for environmental interaction. *Sci. Robot.* **8**, eadh7852 (2023).
13. Cianchetti, M., Laschi, C., Menciassi, A. & Dario, P. Biomedical applications of soft robotics. *Nat. Rev. Mater.* **3**, 143–153 (2018).
14. Kim, Y., Parada, G. A., Liu, S. & Zhao, X. Ferromagnetic soft continuum robots. *Sci. Robot.* **4**, eaax7329 (2019).
15. Roche, E. T. *et al.* Soft robotic sleeve supports heart function. *Sci. Transl. Med.* **9**, eaaf3925 (2017).
16. Buchner, T. J. K. *et al.* Vision-controlled jetting for composite systems and robots. *Nature* **623**, 522–530 (2023).
17. Lacour, S. P., Courtine, G. & Guck, J. Materials and technologies for soft implantable neuroprostheses. *Nat. Rev. Mater.* **1**, 16063 (2016).
18. Joo, H. *et al.* Soft implantable drug delivery device integrated wirelessly with wearable devices to treat fatal seizures. *Sci. Adv.* **7**, eabd4639 (2021).
19. Laschi, C. *et al.* Soft robot arm inspired by the octopus. *Adv. Robot.* **26**, 709–727 (2012).
20. Renda, F., Giorelli, M., Calisti, M., Cianchetti, M. & Laschi, C. Dynamic model of a multibending soft robot arm driven by cables. *IEEE Trans. Robot.* **30**, 1109–1122 (2014).
21. Della Santina, C., Katzschmann, R. K., Bicchi, A. & Rus, D. Model-based dynamic feedback control of a planar soft robot: trajectory tracking and interaction with the environment. *Int. J. Rob. Res.* **39**, 490–513 (2020).
22. Pikul, J. H. *et al.* Stretchable surfaces with programmable 3D texture morphing for synthetic camouflaging skins. *Science* **358**, 210–214 (2017).
23. Aubin, C. A. *et al.* Powerful, soft combustion actuators for insect-scale robots. *Science*

381, 1212–1217 (2023).
24. Xin, C. *et al.* Environmentally Adaptive Shape-Morphing Microrobots for Localized Cancer Cell Treatment. *ACS Nano* **15**, 18048–18059 (2021).
25. Miskin, M. Z. *et al.* Electronically integrated, mass-manufactured, microscopic robots. *Nature* **584**, 557–561 (2020).
26. Kollipara, P.S., Li, X., Li, J. *et al*. Hypothermal opto-thermophoretic tweezers. *Nat. Commun.* **14**, 5133 (2023).
27. Pang, W. *et al*. A soft microrobot with highly deformable 3D actuators for climbing and transitioning complex surfaces. *Proc. Natl. Acad. Sci.* **119**, e2215028119 (2022).
28. Hwang, D., Barron, E. J., Tahidul Haque, A. B. M. & Bartlett, M. D. Shape morphing mechanical metamaterials through reversible plasticity. *Sci. Robot.* **7**, eabg2171 (2022).
29. Bai, Y. *et al.* A dynamically reprogrammable surface with self-evolving shape morphing. *Nature* **609**, 701–708 (2022).
30. Ko, J. *et al.* High-performance electrified hydrogel actuators based on wrinkled nanomembrane electrodes for untethered insect-scale soft aquabots. *Sci. Robot.* **7**, eabo6463 (2022).
31. Li, G. *et al.* Self-powered soft robot in the Mariana Trench. *Nature* **591**, 66–71 (2021).
32. Wang, X. *et al.* Untethered and ultrafast soft-bodied robots. *Commun. Mater.* **1**, 67 (2020).
33. Gu, H. *et al.* Self-folding soft-robotic chains with reconfigurable shapes and functionalities. *Nat. Commun.* **14**, 1263 (2023).
34. Kim, Y., Yuk, H., Zhao, R., Chester, S. A. & Zhao, X. Printing ferromagnetic domains for untethered fast-transforming soft materials. *Nature* **558**, 274–279 (2018).
35. Ren, Z., Hu, W., Dong, X. & Sitti, M. Multi-functional soft-bodied jellyfish-like swimming. *Nat. Commun.* **10**, 2703 (2019).
36. Ozcelik, A. *et al.* Acoustic tweezers for the life sciences. *Nat. Methods* **15**, 1021–1028 (2018).
37. Ma, Z. *et al.* Spatial ultrasound modulation by digitally controlling microbubble arrays. *Nat. Commun.* **11**, 4537 (2020).
38. Del Campo Fonseca, A. *et al.* Ultrasound trapping and navigation of microrobots in the mouse brain vasculature. *Nat. Commun.* **14**, 5889 (2023).
39. Deng, Y., Paskert, A., Zhang, Z., Wittkowski, R. & Ahmed, D. An acoustically controlled helical microrobot. *Sci. Adv.* **5260**, eadh5260 (2023).
40. Marzo, A. *et al.* Holographic acoustic elements for manipulation of levitated objects. *Nat. Commun.* **6**, 8661 (2015).
41. Zhang, Z., Sukhov, A., Harting, J., Malgaretti, P. & Ahmed, D. Rolling microswarms along acoustic virtual walls. *Nat. Commun.* **13**, 7347 (2022).
42. Dillinger, C., Nama, N. & Ahmed, D. Ultrasound-activated ciliary bands for microrobotic systems inspired by starfish. *Nat. Commun.* **12**, 6455 (2021).
43. Zhang, Z., Shi, Z. & Ahmed, D. SonoTransformers : Ultrafast Transformable Wireless Microscale Machines. *arxiv*. (2023)
44. Janiak, J., Li, Y., Ferry, Y., Doinikov, A. A. & Ahmed, D. Acoustic microbubble propulsion, train-like assembly and cargo transport. *Nat. Commun.* **14**, 4705 (2023).
45. Durrer, J. *et al.* A robot-assisted acoustofluidic end effector. *Nat. Commun.* **13**, 6370 (2022).
46. Jooss, V. M., Bolten, J. S., Huwyler, J. & Ahmed, D. In vivo acoustic manipulation of microparticles in zebrafish embryos. *Sci. Adv.* **8**, eabm2785 (2022).
47. Prakash, M. & Gershenfeld, N. Microfluidic Bubble Logic. *Science* **315**, 832-835 (2007).
48. Leighton, T. Applications of One-Dimensional Bubbles to Lithotripsy and to Diver

Response to Low Frequency Sound. *Acta Acust.* **3**, 517–529 (1995).
49. Wei, W., Thiessen, D. B. & Marston, P. L. Acoustic radiation force on a compressible cylinder in a standing wave. *J. Acoust. Soc. Am.* **116**, 201–208 (2004).
50. Williams, A. *Structural analysis: In theory and practice*. *Structural Analysis: In Theory and Practice* (2008).
51. H. N. Oğuz, A. Prosperetti, The natural frequency of oscillation of gas bubbles in tubes. *J. Acoust. Soc. Am.* **103**, 3301-3308 (1998).
52. C. P. Lee, T. G. Wang, Acoustic radiation force on a bubble. *J. Acoust. Soc. Am.* **93**, 1637-1640 (1993).
53. D. L. Miller, A cylindrical-bubble model for the response of plant-tissue gas bodies to ultrasound. *J. Acoust. Soc. Am.* **65**, 1313-1321 (1979).
54. P. M. C. Morse, K. U. Ingard, P. M. Morse, *Theoretical Acoustics*. (McGraw-Hill, 1968).
55. L. Brillouin, *Tensors in Mechanics and Elasticity*. (Academic Press, 1964).

Acknowledgments: This project was funded by the European Research Council (ERC) under the European Union's Horizon 2020 research and innovation program (grant agreement No. 853309, SONOBOTS); the Swiss National Science Foundation (SNSF) through the SNSF Project funding MINT 2022 (grant agreement No. 213058), Spark Grant (grant agreement No. 221285); and the ETH Research Grant (grant agreement No. ETH-08 20-1). Z.S. acknowledges financial support from the China Scholarship Council (202106320193). Z.Z. acknowledges financial support from the China Scholarship Council (202006210065). We thank the operational team of the clean room facility in the Binnig and Rohrer Nanotechnology Center (BRNC) for their helpful discussion on the fabrication wafer. The authors thank Dan Schoenenberger for his helpful contribution to the initial fabrication and testing.

Author contributions: D.A. conceived and supervised the project. Z.S and Z.Z. developed the design and fabrication of prototypes, performed experiments and data analysis. Z.S., Z.Z., and D.A. contributed to the theoretical understanding. Z.S. contributed to the numerical simulations. Z.Z., Z.S., and D.A. contributed to the scientific presentation, discussion, and manuscript revision. Competing interests: Authors declare that they have no competing interests.

Competing interests: The authors declare that they have no competing interests.

Data and materials availability: All data needed to evaluate the conclusions in the paper are present in the paper and/or the Supplementary Materials.

Supplementary Materials for

Ultrasound-Driven Programmable Artificial Muscles

Zhan Shi†, Zhiyuan Zhang†, Daniel Ahmed*
Corresponding author: dahmed@ethz.ch

The PDF file includes:

Materials and Methods
Supplementary Text
Supplementary Figs. S1 to S9
Legends for Supplementary Movies S1 to S7

Other Supplementary Materials for this manuscript include the following:

Movies S1 to S7

Materials and Methods

1. Fabrication of artificial muscles

The negative patterns of artificial muscles are first designed in the commercial software LayoutEditor (as shown in **Fig. S1**). The patterns are transferred into a photomask by a direct writing laser (DWL) machine in a cleaning room (BRNC, Ruschlikon, Switzerland). Then, we spin coat the negative photoresist SU8-3025 on a 4-inch silicon wafer. By the standard lithographic fabrication, the patterns are transferred to the photoresist via exposing to UV light through the mask. After the developing process, the negative patterns of the microbubble-arrays, i.e., micropillars, are additive on the wafer. The height of the micropillar depends on the spinning speed. We then fabricate the soft artificial muscles through standard mold-replica techniques. We spin coat PDMS resin (mixed with the curing agent at a 10:1 ratio) on the surface of the wafer and then put the wafer into a vacuum chamber to remove any bubbles. The relationship between the thickness of the PDMS layer and the spinning speed is illustrated in **Fig. S2**. The muscle thickness of 80 ± 10 μm (with 50 μm length microbubbles) and 280 ± 20 μm (with 150 μm length microbubbles) used in the study are obtained with the spinning speed of 400 revolutions per minute (rpm) and 1000 rpm, respectively. The wafer with spin coated PDMS is put into an oven (100 °C) to accelerate the curing process. After curing, the thin PDMS layer is peeled off from the wafer and cut along the outline to get the desired microbubble-array artificial muscles.

2. Acoustic setup

For the microscale characterization of microbubbles, the experimental setup is built on a thin glass substrate with dimensions of 24×60×0.18 mm. As shown in **Fig. S3A**, a circular piezoelectric transducer (27×0.54 mm, resonance frequency 4.6 kHz $\pm$ 4%, Murata 7BB-27-4L0) is affixed to the glass substrate using an epoxy resin (2-K-Epoxidkleber, UHU Schnellfest). A square PDMS acoustic chamber (10×10×5 mm) is positioned in the front of the transducer, which is filled with deionized water and covered with a cover glass (22×22×0.18 mm). The substrate is then mounted on an inverted microscope (Axiovert 200M, ZEISS). For the macroscale actuation of acoustic artificial muscles, the experimental setup is built on a thin plastic tank with dimensions of 10×10×8 cm and a thickness of 2 mm. As shown in **Fig. S5**, the circular piezoelectric transducers are affixed to the inside surfaces and the bottom surface of the tank using the epoxy resin or directly submerged into the liquid because the deionized water filled in the tank is not conductive. Three cameras are placed around the tank to capture the actuation of acoustic artificial muscles from multiple view angles. An electronic function generator (AFG-3011C, Tektronix) and an amplifier ($0-60$ V_{PP}, 15x amplification, High Wave 3.2, Digitum-Elektronik) are connected to the transducer to generate sound waves with tunable excitation frequencies and voltages.

3. Numerical simulations

Finite element numerical simulations are conducted using the commercial COMSOL Multiphysics software (v6.1, Burlington, MA), including simulations on the acoustic pressure field in the small PDMS chamber, the acoustic pressure field in the big acoustic tank, and the deformations of these artificial muscles. All simulations are performed with consistent dimensions and material properties as experiments. Physics modules of simulations on acoustic pressure include the solid mechanics, electrostatics, pressure acoustics fields, creeping flow, and heat transfer in solids and fluids. Simulations on the deformations of artificial muscles are performed using the solid mechanics module with corresponding boundary conditions and force conditions. The microstreaming generated thrust is assumed to a point force which loaded on the bottom of

each microcavity. Additionally, numerical calculations on the theoretical model are performed using the commercial Matlab software (R2022b).

4. Imaging and analysis

The microscale characterization of microbubbles is recorded with a high-speed camera (Chronos 1.4, Kron Technologies) attached to the inverted microscope. Recording frame rates range from 1069 to 32,668 frames per second (fps). The macroscale motion of acoustic artificial muscles is recorded with a high-sensitive camera (Canon 6D and 24−70 mm camera lens, Canon). The recording frame rate is 50 fps. Recorded footages are analyzed in ImageJ.

Supplementary Text
Theoretical modeling and simulations

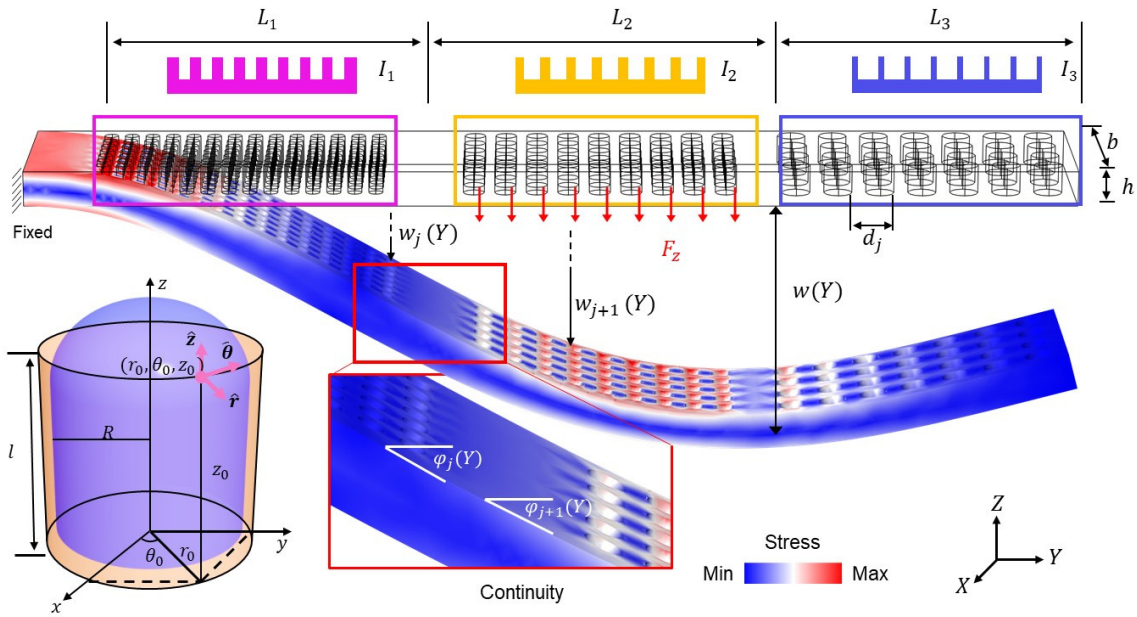

Fig. T1. Modelling of the activation mechanism of microbubble-array artificial muscles. Modelling and simulation of the variable-size microbubbles arrays artificial muscle. The purple, yellow and pink box represent the different sizes microbubble-array element, upper shows the schematic of the cross-section of the artificial muscle, which have corresponding momentum inertia I_j $(j = 1,2,3)$. Inset shows the continuous deformation conditions. F_z denotes the thrust force generated by the microstreaming. $w(Y)$ and $\varphi(Y)$ denote the deflection and rotation angle along the long axis (Y axis). Lower left inset shows the modelling of the microbubble based on the cylinder coordinate.

For an axisymmetric cylinder microbubble (radius R and length l, shown in **Fig. T1**) surrounded by fluid with the density ρ_0 and sound speed c_0, the natural resonance frequency is estimated as $f_0 = \frac{1}{2\pi}\sqrt{\frac{3\pi\gamma P_0}{8rl\rho_0}}$, where γ is the adiabatic index (1.4 for air), P_0 is the atmospheric pressure (*51*) . When this microbubble is excited by sound waves with a frequency ω, the surface of the microbubble oscillates and generates a plane wave traveling along the z-axis. This wave will generate a complex acoustic pressure $\boldsymbol{P} = \boldsymbol{P}_{\mathrm{i}0}e^{-\mathrm{i}\omega t}$, where i is the imaginary unit (*52*). The time-independent factor $\boldsymbol{P}_{\mathrm{i}0}$ is

$$\boldsymbol{P}_{\mathrm{i}0} = \boldsymbol{P}_a e^{\mathrm{i}k_0 z} = \boldsymbol{P}_a \sum_{n=0}^{\infty} \epsilon_n \mathrm{i}^n J_n(k_0 r)\cos(n\theta) \tag{1}$$

where $\boldsymbol{P}_a$ is the amplitude of the acoustic pressure. $\epsilon_n = 2 - \delta_{0n}$, and δ_{0n} is the Kronecker delta. n is the nth order of the cylindrical Bessel function J_n (*53*), which is corresponding to the oscillation modal shapes of the bubble, and $k_0 = \omega/c_0$. In this work, the simulated first order shape of the Bessel function coordinates with the experimentally measured oscillation shapes of a single microbubble (as shown in **Fig. 4A),** thus $n = 1$ in our experiments. However, we still keep the n in the following derivation, which can provide more insights in the future work related to other higher oscillation modes of the microbubbles. The scattered wave field, must look like an

outgoing wave when the cylinder coordinate $r \to \infty$ (*54*); therefore Eq. (1) can be expanded as a sum of cylindrical Hankel functions H_n

$$\boldsymbol{P}_{\mathrm{i}0} \approx \boldsymbol{P}_a \sum_{n=0}^{\infty} \epsilon_n \mathrm{i}^n a_n H_n^{(1)}(k_0 r)\cos(n\theta) \tag{2}$$

where a_n is the dimensionless scattering coefficients for each partial wave and can be determined from the boundary condition at the surface of the cylinder.

The total acoustic velocity potential is related to the complex acoustic pressure by $\boldsymbol{\Phi} = \frac{\boldsymbol{P}}{i\omega\rho_0} = \boldsymbol{\Phi}_0 e^{-\mathrm{i}\omega t}$, which conforms the following approximation

$$\lim_{k_0 r \to \infty} \boldsymbol{\Phi}_0 = \boldsymbol{\Phi}_{\mathrm{i}0} + \frac{\eta(\theta)}{\sqrt{k_0 r}} e^{\mathrm{i}k_0 r} \tag{3}$$

where $\boldsymbol{\Phi}_{\mathrm{i}0} = \frac{P_{\mathrm{i}0}}{\mathrm{i}\omega\rho_0}$, and $\eta(\theta)$ is the coefficient which is determined from the boundary conditions at the surface of the cylinder microbubble. Considering the long-wavelength approximation of Yosioka and Kawasima, the acoustic radiation force is given by following the integral over the closed surface $\boldsymbol{A}$ of the microbubble:

$$\boldsymbol{F} = \oint_{\boldsymbol{A}} \boldsymbol{S}_T \cdot d\boldsymbol{A} \tag{4}$$

where $\boldsymbol{S}_T = (\langle \boldsymbol{K} \rangle - \langle \boldsymbol{V} \rangle)\boldsymbol{I} - \rho_0 \langle \boldsymbol{u}\boldsymbol{u} \rangle$ is the Brillouin stress tensor (*55*) , in which $\langle \boldsymbol{K} \rangle = (\rho_0/2)\langle \boldsymbol{u}^2 \rangle$ is the local average of the acoustic kinetic energy density, $\langle \boldsymbol{V} \rangle = \langle \boldsymbol{p}^2 \rangle/(2\rho_0 c_0^2)$ is the local average of the acoustic potential energy density, and $\boldsymbol{I}$ is the unit tensor. $\boldsymbol{u} = \nabla(\mathrm{Re}(\boldsymbol{\Phi}))$ and $\boldsymbol{p} = -\rho_0 \frac{\partial(\mathrm{Re}(\boldsymbol{\Phi}))}{\partial t}$ are the acoustic particle speed field and pressure. The resultant net force will only have the z component due to the symmetry of the cylinder microbubble, so

$$\begin{aligned} F_z &= \boldsymbol{F} \cdot \hat{\boldsymbol{e}}_{\boldsymbol{z}} \\ &= -\oint_{S_r} \rho_0 \hat{\boldsymbol{e}}_{\boldsymbol{z}} \cdot \langle \boldsymbol{u}\boldsymbol{u} \rangle \cdot \mathrm{d}\boldsymbol{A} + \oint_{S_r} \left\{ \frac{\rho_0}{2} \langle |\boldsymbol{u}|^2 \rangle - \frac{1}{2\rho_0 c_0^2} \langle \boldsymbol{p}^2 \rangle \right\} \mathrm{d}\boldsymbol{A} \cdot \hat{\boldsymbol{e}}_{\boldsymbol{z}} \end{aligned} \tag{5}$$

Equation (5) gives the expressions of the acoustic streaming force generated by a single microbubble, which is relevant to the dimensions of the microbubble (radius r and length l), the surround fluid property (density ρ_0 and sound wave speed c_0), the boundary conditions of the surface of the microbubble (the coefficients a_n and $\eta(\theta)$), and the vibration amplitude of the microbubble surface, which is determined by the input voltage and the sound wave transmission distance and efficiency.

The schematic and simulations of the variable-size microbubble-array artificial muscle is shown in **Fig. T1**, which is divided into three different segments j ($j = 1,2,3$) based on the radii (R_j) of the microbubble-arrays. The rotational momentum inertia I_{j} of each region is determined by the microcavities' dimensions, quantities, and distances. It is assumed that microbubbles with the consistent radius are excited and quiescent simultaneously when turning on or off the ultrasound, and should have the consistent force F_{z_j}, Thus the propulsion force exerted on the artificial muscles' specific segment can be estimated as a uniform distributed load $F_{u_j} = N_j F_{z_j}/S_j$, where N_j and S_j are the number of the specific size bubbles and its corresponding region's area. Based on the above assumptions and in the framework of Euler-Bernoulli theories (*50*), the governing equation of the beam is

$$\delta(V_m + V_b - W) = 0 \tag{6}$$

where

$$V_m = \int_V \Psi \mathrm{d}V = \int_{V_j} \Psi \mathrm{d}V_j \text{ , } (j = 1,2,3)$$

$$V_b = \frac{1}{2}EI_1 \int_0^{L_1} {\varphi_1}'^2 \mathrm{d}x + \frac{1}{2}EI_2 \int_{L_1}^{L_1+L_2} {\varphi_2}'^2 \mathrm{d}x + \frac{1}{2}EI_3 \int_{L_1+L_2}^{L_1+L_2+L_3} {\varphi_3}'^2 \mathrm{d}x$$

$$W = \int_0^{L_1} F_{u1}(t) w_1 \mathrm{d}x + \int_{L_1}^{L_1+L_2} F_{u2}(t+\tau_1) w_2 \mathrm{d}x + \int_{L_1+L_2}^{L_1+L_2+L_3} F_{u3}(t+\tau_2) w_3 \mathrm{d}x$$

V_m and V_b are the body strain energy and the bending strain energy, respectively. W is the external load. Ψ is the energy density function. E is the Young's modulus of the material. $\varphi(X,t)$ is the rotation angel along the beam. L_j is the length of the jth segment. τ_1 and τ_2 are the time delays between two sequential microbubbles' excitation frequencies. V_j represents the volume of each segment, which equals $V_j = A_c L_j - N_j \pi R_j^2 l$, where $A_c = bh$ is the cross-section area of the artificial muscle, while b and h are the width and thickness.

Equation 7 reveals the variable-size microbubble-array artificial muscles' transient deformation behavior which can be solved by

$$\begin{aligned}
w_1(x) &= \frac{x^2}{24EI_1}(x^2 + 6L_1^2 - 4L_1 x)\ (0 \le x \le L_1) \\
\varphi_1(x) &= \frac{x}{6EI_1}(3L_1^2 - 3L_1 x + x^2)(0 \le x \le L_1) \\
w_2(x) &= \frac{(x-L_1)^2}{24EI_2}(L_1 + L_2 - x)^2\ (L_1 < x \le L_2) \\
\varphi_2(x) &= \frac{x}{12EI_1}(L_1 + L_2 - x)(2L_1 + L_2 - 2x)(L_1 < x \le L_2) \\
w_3(x) &= \frac{x^2}{24EI_3}(x^2 + 6(L_3 - L_2)^2 - 4(L_3 - L_2)x)\ (L_2 < x \le L_3) \\
\varphi_3(x) &= \frac{x}{6EI_3}(3L_3^2 - 3L_3(x - L_1 - L_2) + (x - L_1 - L_2)^2)(L_2 < x \le L_3)
\end{aligned} \tag{7}$$

However, according to the deflection and rotation continuity (**Fig. T1**), the deformation of the whole artificial muscle should conform the following boundary conditions: $w_1(L_1) = w_2(L_1)$, $w_2(L_2) = w_3(L_2)$ and $\varphi_1(L_1) = \varphi_2(L_1)$, $\varphi_2(L_2) = \varphi_3(L_2)$.

The governing equation of the variable-size microbubble-array artificial muscle can be transformed to uniform-size microbubble-array artificial muscle by making L_2 and L_3 equal 0. To verify the developed model, we give an example which use the above equations to calculate the deformation of the uniform-size microbubble-array artificial muscle, and the calculation match well with the experiments, as shown in **Fig. T2**. In this theoretical calculation, Young's Modulus (E) is 1×10^7 Pa; Applied uniform distributed load ranges from 0 to 1000 μN; Length of the artificial muscle (L) is 3×10^{-2} m; Moment of inertia (I) is 3×10^{-13} m^{-4}.

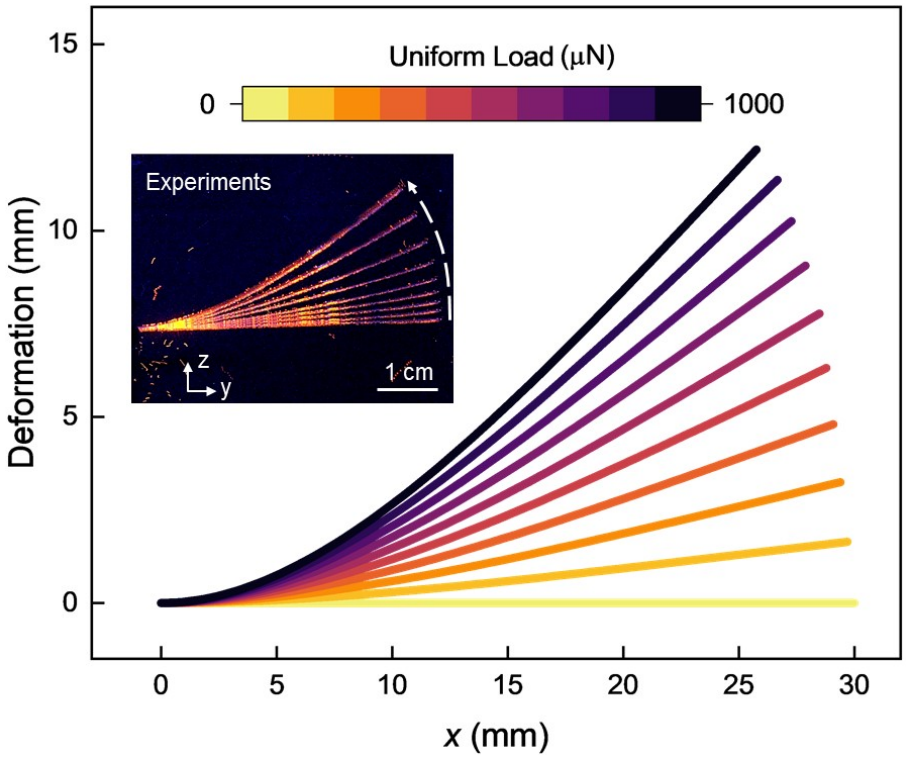

Fig. T2. Theoretical calculations of deformation of a uniform-size microbubble-array artificial muscle. The calculation was performed using Matlab R2022b and employed Equation (7) as the basis.

Supplementary Figures

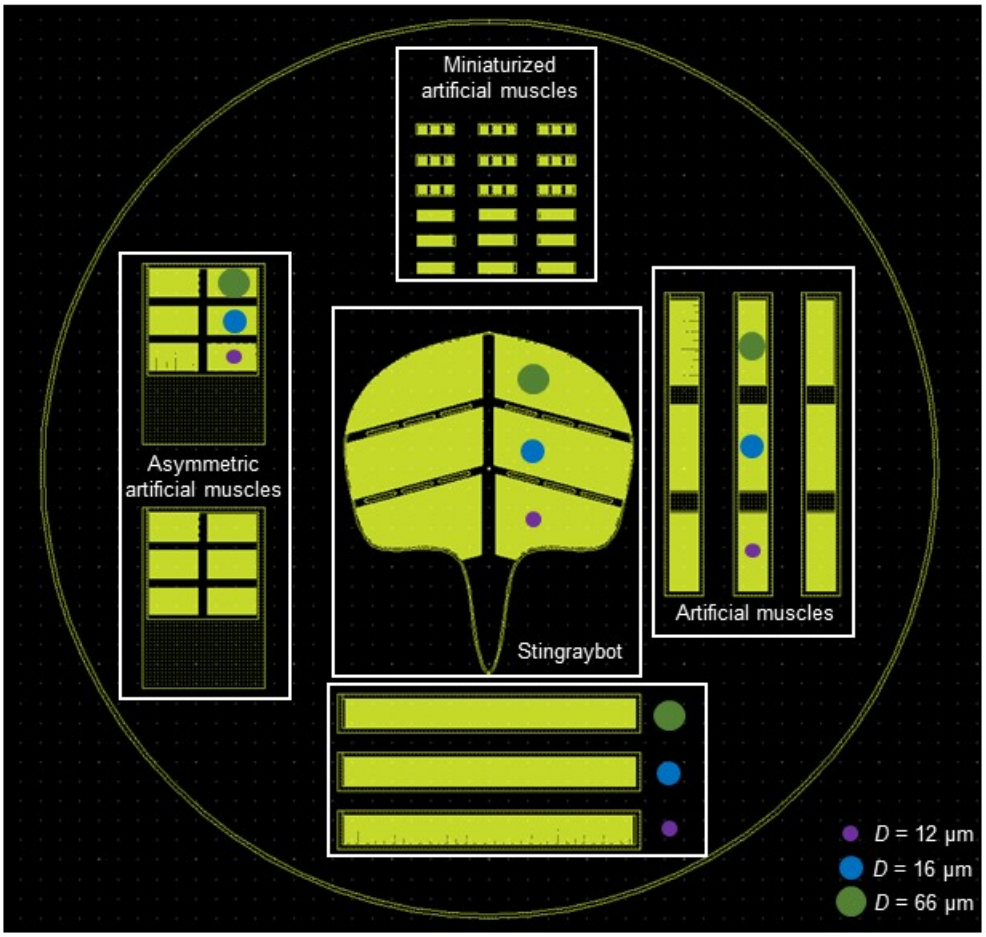

Fig. S1. Design of artificial muscles and stingraybot. At the center of the 4-inch wafer profile, a bioinspired stingraybot is depicted, comprising three distinct microbubble-arrays with varying radii arranged from the head to the tail. At the bottom are three artificial muscles with uniform-size microbubble-arrays. On the right are the artificial muscles with variable-size microbubble-arrays. Both the artificial muscles at the bottom and the right side are 30 mm in length and 5 mm in width. The top presents the miniaturized artificial muscles, which are scaled down by ×0.12 of the muscles at the bottom and the right. However, the microbubbles of these miniaturized artificial muscles are kept with the same radii. On the left are the artificial muscles with asymmetric arrangement of microbubble-arrays. The magenta, blue, and green circles denote the diameters of microbubble of 60 μm, 18 μm, and 12 μm, respectively.

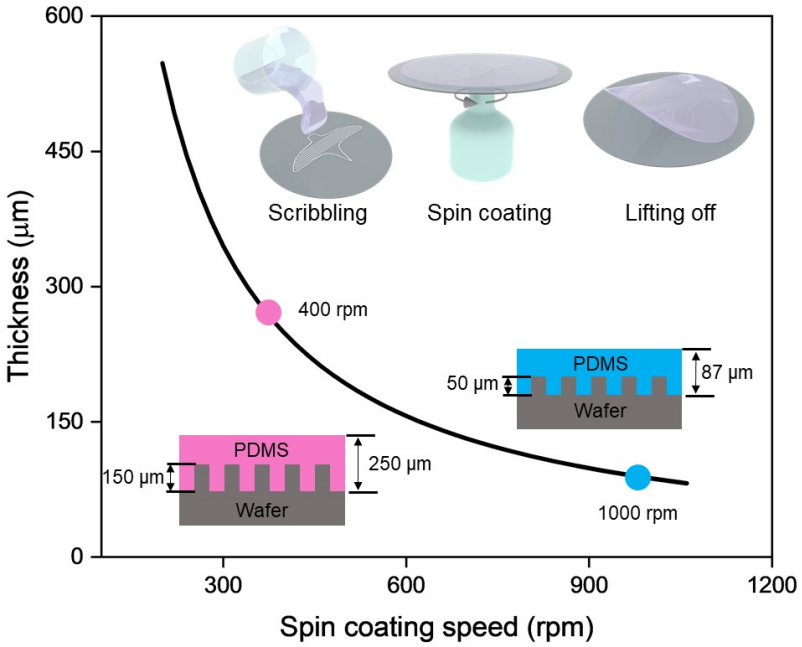

Fig. S2. Artificial muscle thickness versus PDMS spin coating speed. The black curve illustrates the resulting thickness of the artificial muscle decreases with a higher spinning speed. The spinning speeds utilized in experiments are highlighted by two specific data points: The pink dot corresponds to a spinning speed of 400 rpm, which was employed on a wafer with 150 μm pillars, resulting in a thicker thickness of 250 μm for the artificial muscle. The blue dot represents a spinning speed of 1000 rpm, which was applied to a wafer with 50 μm pillars, yielding a thinner artificial muscle with a thickness of 87 μm. Insets demonstrate the fabrication processing.

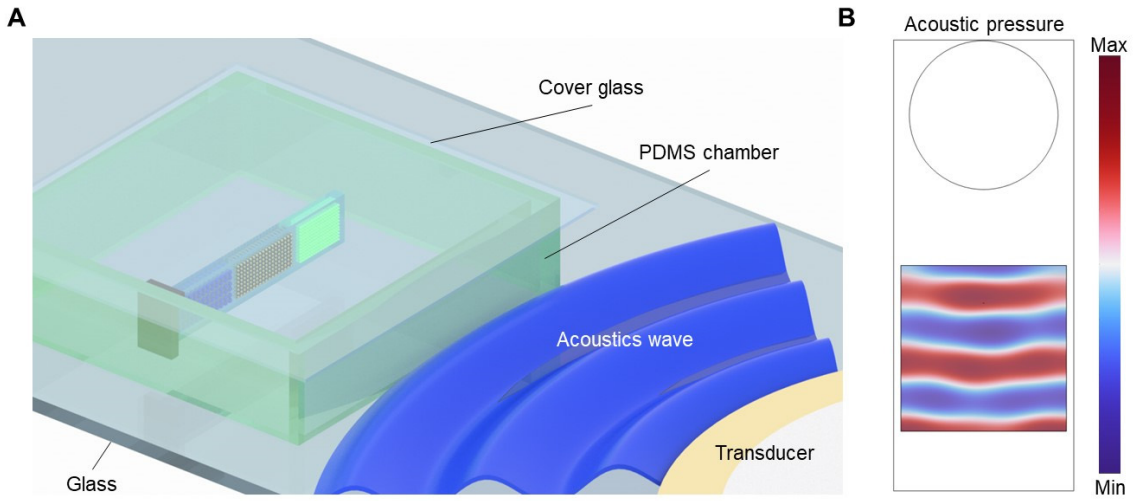

Fig. S3. Experimental setup for microscope characterization of microbubble-arrays and corresponding acoustic pressure field simulation. (**A**) Experimental Setup. A transducer is affixed to the glass slide to generate sound waves and a PDMS chamber is placed in front of the transducer. The artificial muscle is clamped to the wall of the PDMS chamber. The chamber is filled with deionized water and sealed with a cover glass. (**B**) Simulation of the acoustic pressure distribution in the chamber.

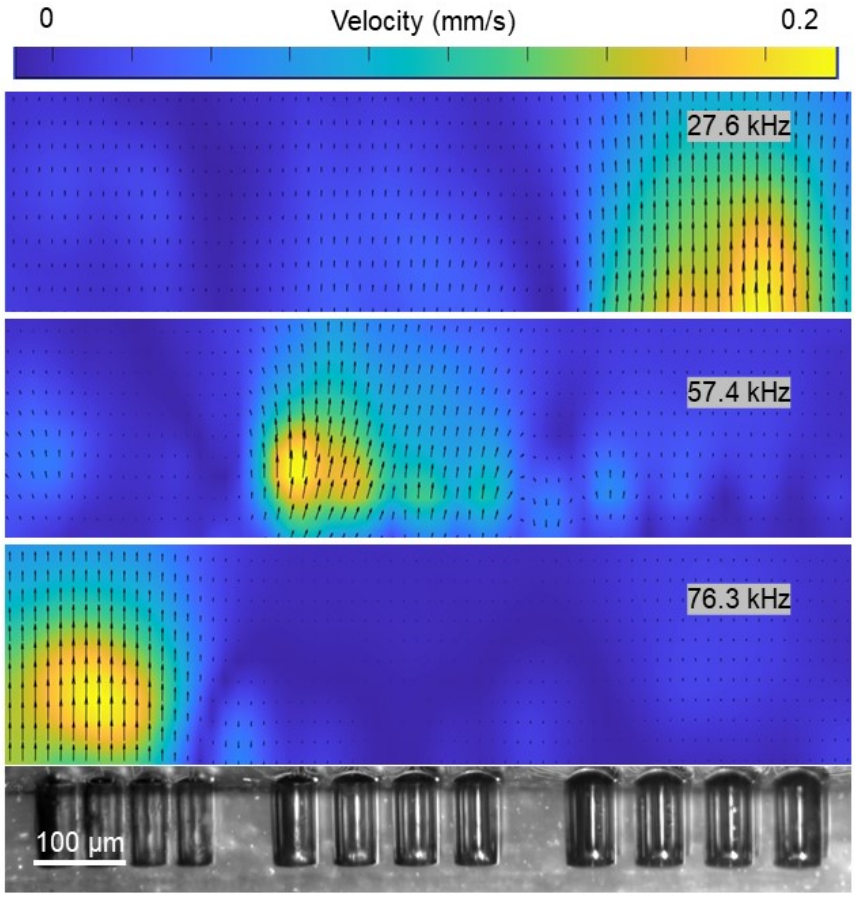

Fig. S4. Measurement of microstreaming velocity by PIV. The microbubbles from left to right are with radii of 20 μm, 30 μm, and 40 μm, respectively. Each set of microbubbles measures 4×4 and has a length of 150 μm. When keeping the ultrasound excitation voltage of 30 V_{PP}, these microbubble-arrays demonstrated distinguished selective excitation at different ultrasound excitation frequencies of 27.6 kHz, 57.4 kHz, and 76.3 kHz. Microparticles with a 2 μm diameter were employed as streaming tracers. The streaming flow field was analyzed by particle imaging velocimetry (Matlab R2022b, PIVlab 2.60). Color bar denotes the particle moving velocity.

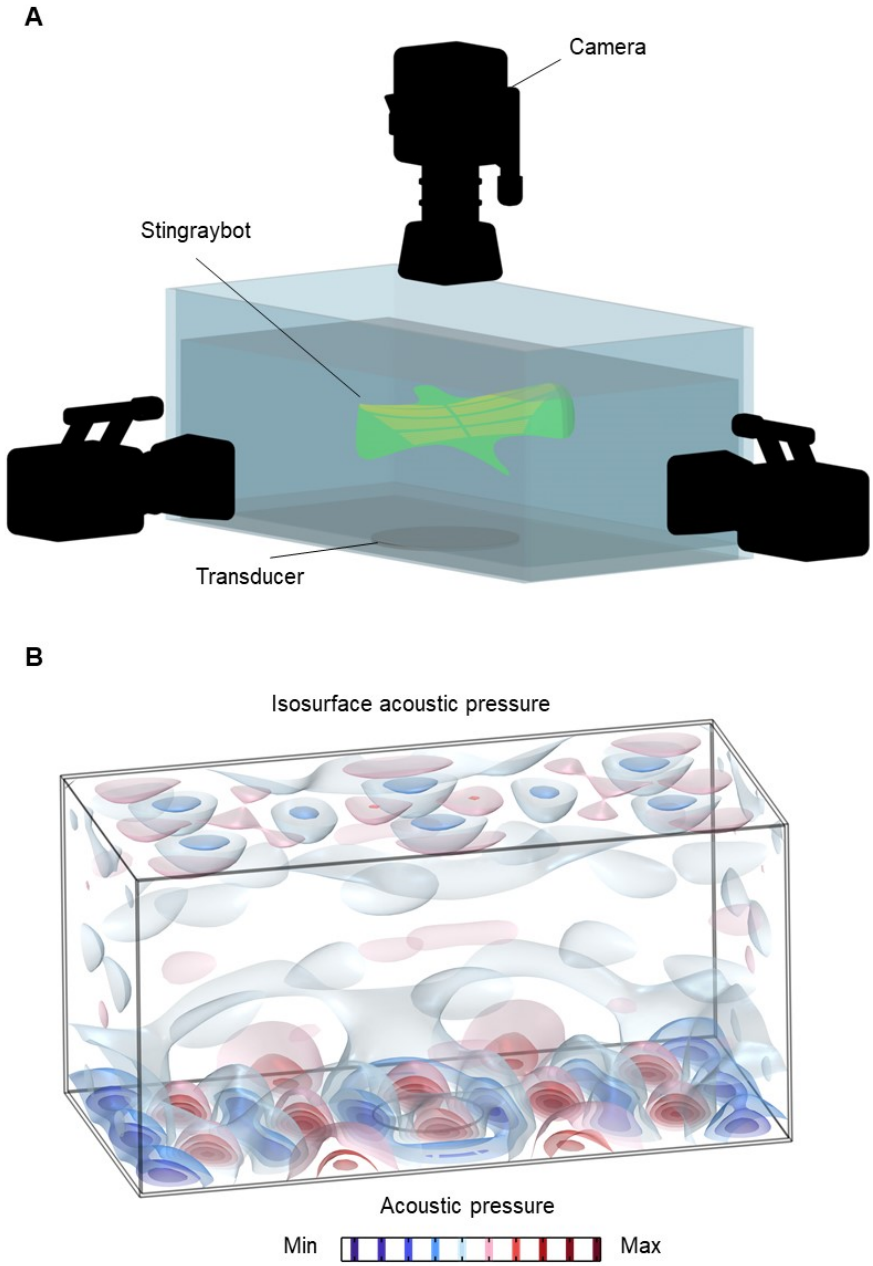

Fig. S5. Experimental setup for artificial muscle actuation and corresponding acoustic pressure field isosurface simulation. (**A**) Experimental Setup. The acoustic tank is filled with deionized water. Three cameras are positioned at the top, left, and front to capture the motion of the bioinspired stingraybot. Transducers are affixed to the bottom of the tank's wall. (**B**) Simulation of acoustic pressure isosurface within the tank conducted using COMSOL Multiphysics V6.1.

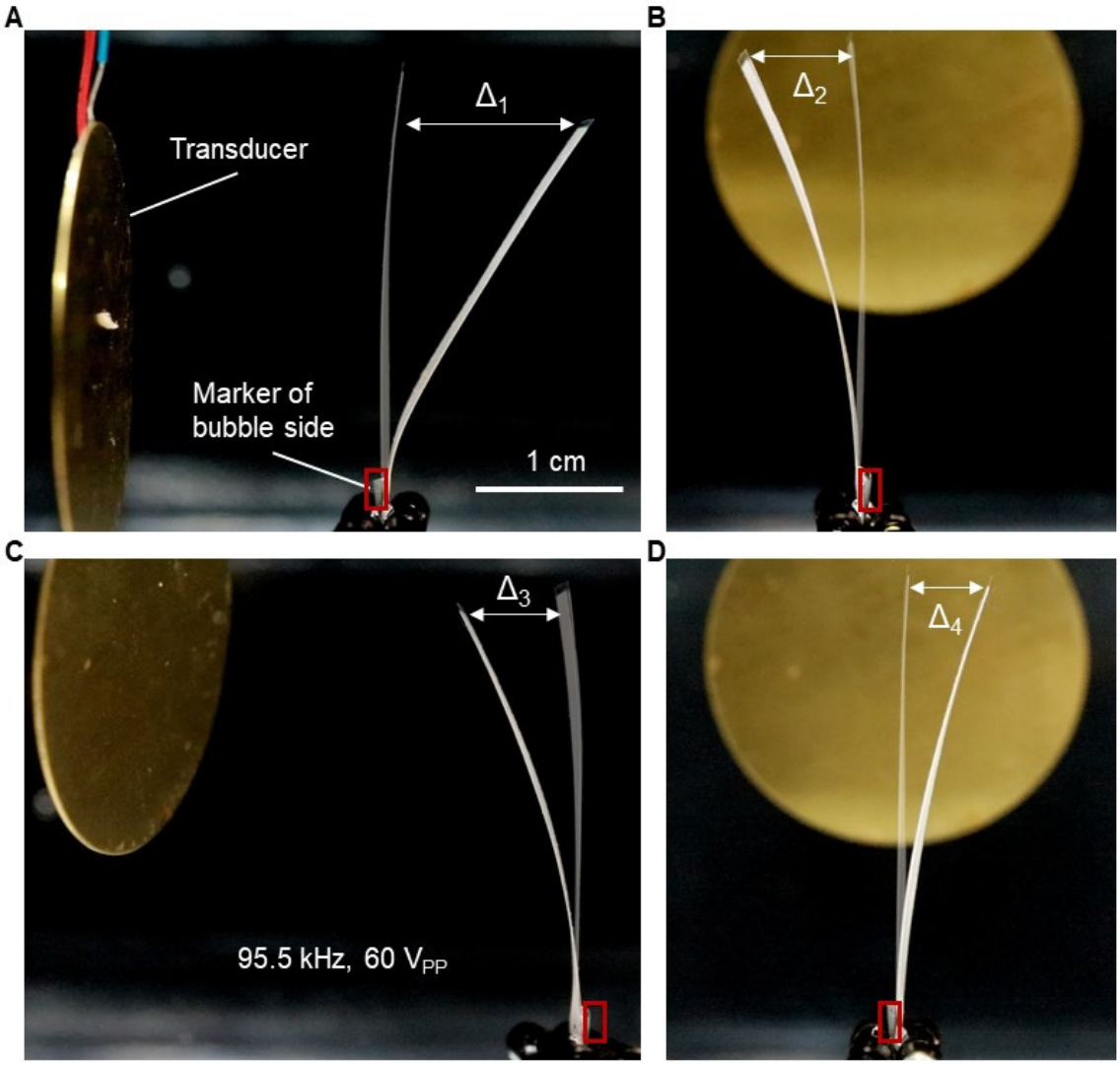

Fig. S6. Displacements of uniform-size microbubble-array artificial muscle with various transducer positions. (**A**) to (**D**) depict the deformations of the uniform-size microbubble-array artificial muscle with different transducer placements, which include positioning the transducer on the opposite, left, back, and right sides of the microbubble-array. The side with microbubble-array is marked by red rectangular. The muscle demonstrated a consistent bending direction regardless of these positions, i.e., all samples bent in the direction opposite to the microbubble-array side, despite the variations in bending amplitudes. The ultrasound excitation is at 95.5 kHz and 60 V_{PP}.

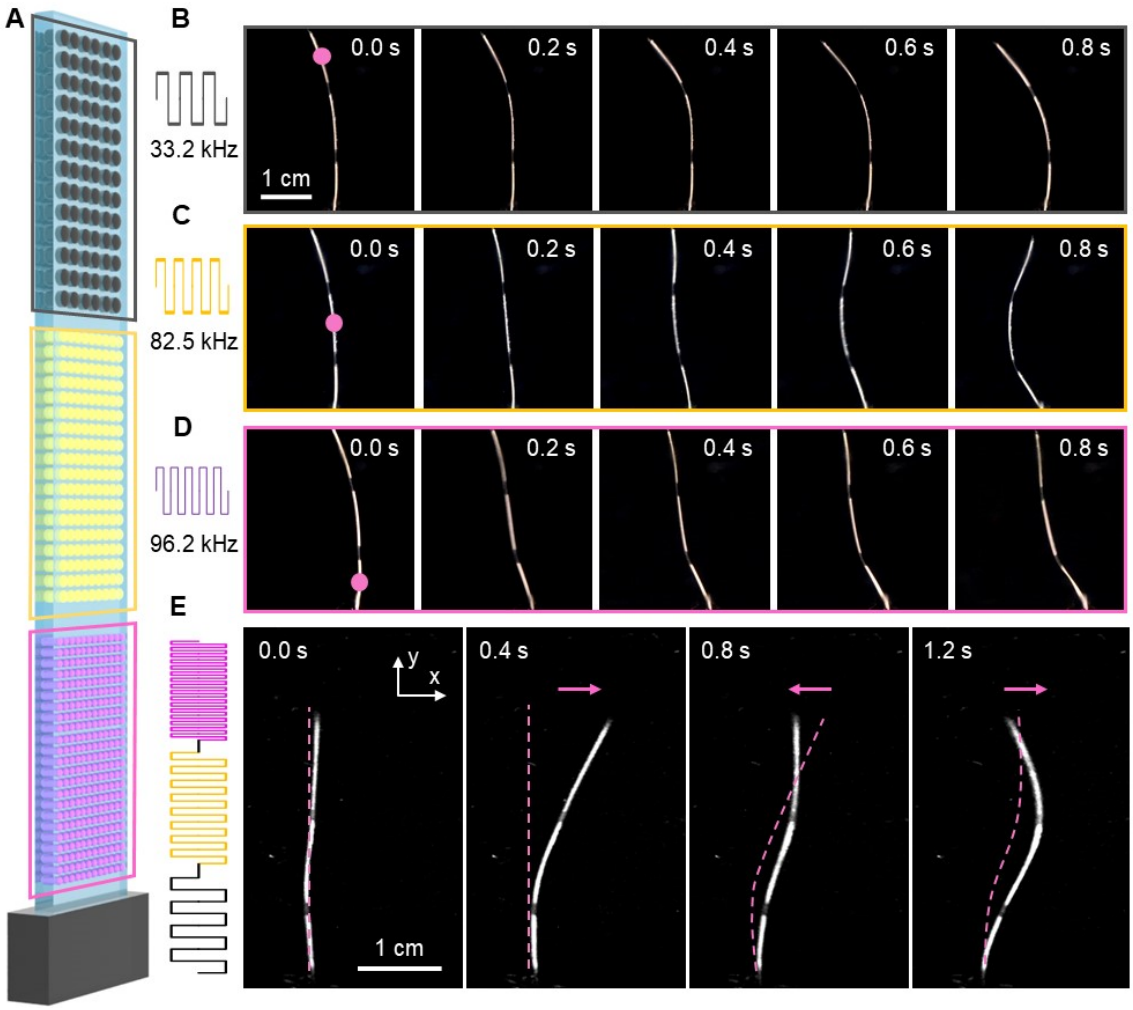

Fig. S7. Deformation of a variable-size microbubble-artificial muscle under constant and sweeping frequency ultrasound excitation. (A) Schematic of the variable-size microbubble-array artificial muscle, comprising three different sizes of microbubble-arrays, denoted by black, yellow, and pink colors. (**B**) to (**D**) Time-lapse sequences of the artificial muscle's deformation when respectively excited the top, middle, and bottom microbubble-arrays, each corresponding to a specific frequency indicated by a color-coded square signal. The magenta dot denotes the excited microbubble-array. (**E**) A time-lapse sequence of the artificial muscle's response to sweeping frequency ultrasound excitation, ranging from 30 kHz to 90 kHz, over a sweeping time of 1.8 seconds. The magenta arrow denotes the deformation direction. The magenta dotted line denotes the posture of the artificial muscle at the previous time point. The ultrasound excitation voltage for all panels are kept at 60 V_{PP}.

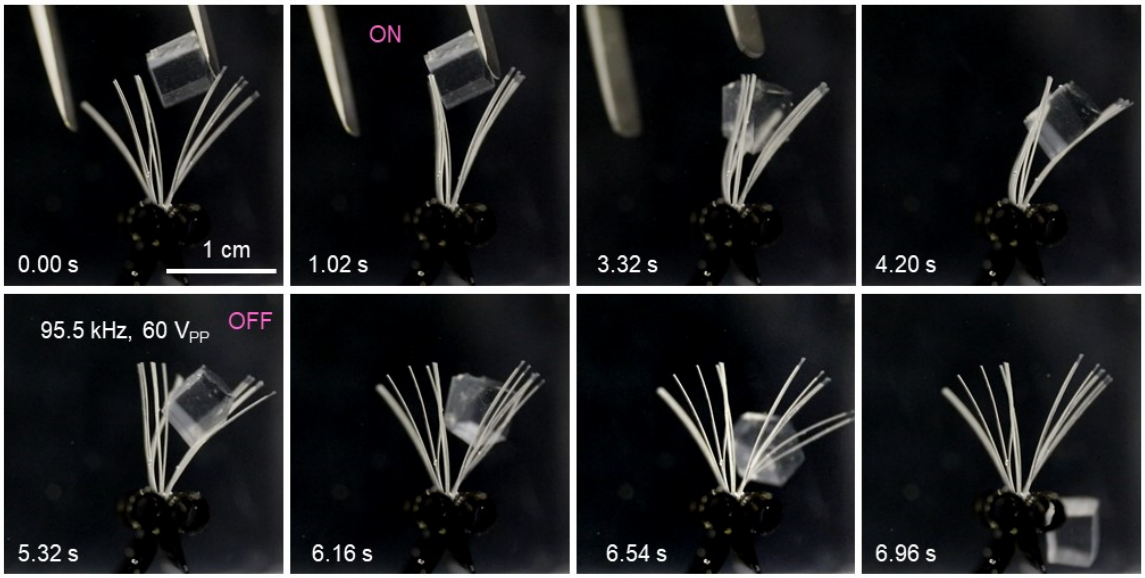

Fig. S8. A microbubble-array soft gripper captured a 35 times heavier PDMS block. The gripper is 7 mg and the PDMS block is 250 mg. The soft gripper comprises of 10 uniform-sized microbubble-array artificial muscle, each of them housed >20000 microbubbles with the diameter of 12 μm. The ultrasound excitation frequency and voltage are 95.5 kHz and 60 V_{PP}.

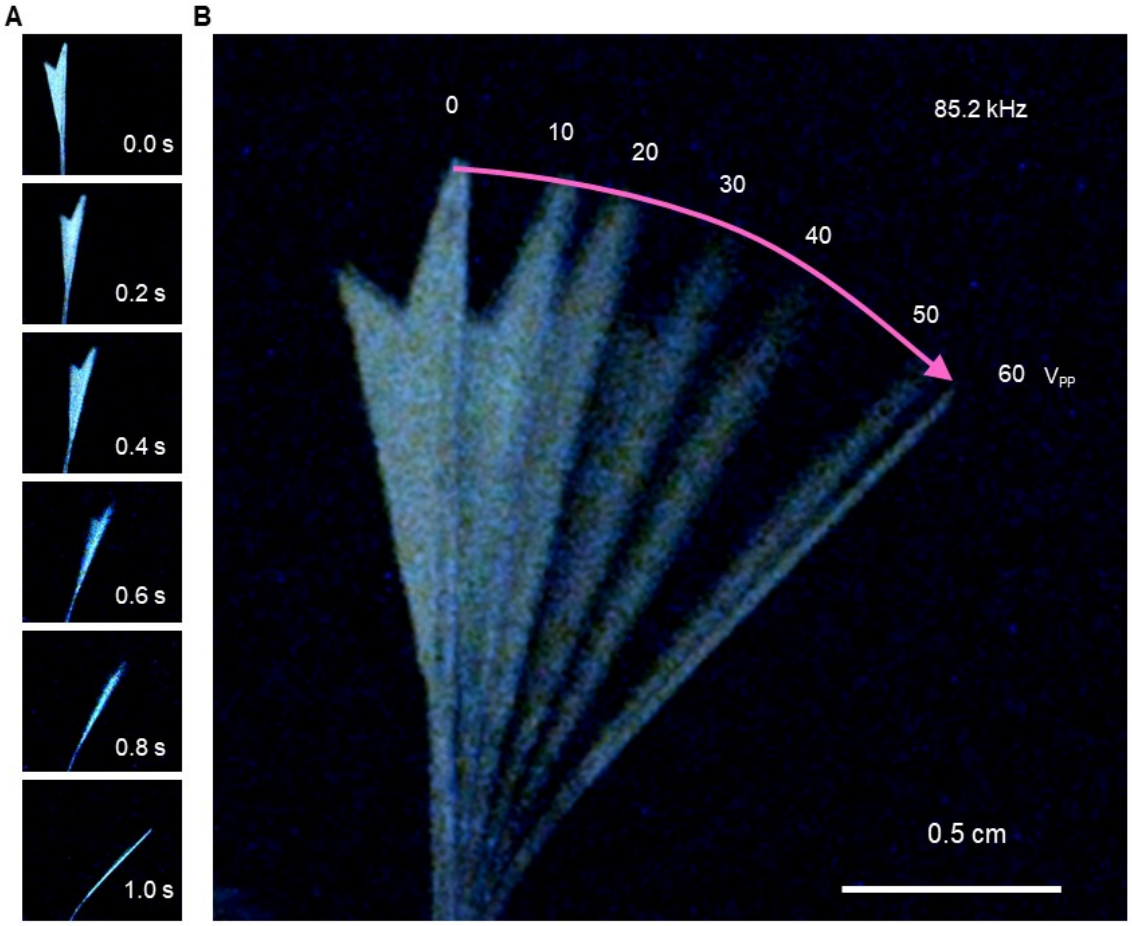

Fig. S9. Deformation of a robotic shark tail with the uniform-size microbubble-array artificial muscle. (A) Time-lapse deformation of the shark tail over a 1 second time ultrasound excitation. The input signal is at 85.2 kHz and 60 V_{PP}. **(B)** Superpositioned deformation of the shark tail with voltage increased from 0 to 60 V_{PP}, while maintaining a constant frequency of 85.2 kHz. The magenta arrow denotes the deformation direction with the microbubble-array on the left side of the shark tail.

Legends for Supplementary Movies

Movie S1. Microscope characterization of the microbubble-arrays.

(**I**) Acoustic streaming under different ultrasound excitation voltages. The microbubble-array contains 4×4 microbubbles with a radius of 60 μm. The left and right videos correspond to 10 V_{PP} and 30 V_{PP} input voltages, respectively, at a frequency of 27.6 kHz. The microparticles used are 3 μm in radius. (**II**) Frequency selectivity of different sizes microbubbles. Microstreaming respectively generated by (40, 60, and 80 μm)×150 μm microbubble-arrays under ultrasound frequencies of 27.6 kHz, 57.4 kHz and 76.3 kHz. (**III**) Response of different sizes microbubbles under sweep-frequency ultrasound excitation. The actuation is achieved by sweeping the frequency within the range of 60-90 kHz, with a sweep time of 1.8 seconds each cycle, and an input voltage of 60 V_{PP}. (**IV**) Acoustic streaming generated deformation. Without microbubbles, the input voltage and frequency are 30 V_{PP} and in the range of 1−90 kHz, with a sweeping time of 3 seconds per cycle. For microbubbles with a radius of 120 μm, the input voltage is 30 V_{PP}, and the frequency matches their natural frequency at 9.5 kHz.

Movie S2. Characterization of uniform-size microbubble-array artificial muscles.

(**I**) Deformation with microbubbles at different locations. Operation at random location. The deformations of the uniform-size microbubble-array artificial muscle resulting from different transducer placements, including positioning the transducer on the opposite, back, left, and right sides of the microbubble-array. The microbubble-array side is indicated by the red rectangle. The input signal utilized for these experiments is 60 V_{PP} at 95.5 kHz. (**II**) Control experiments without microbubbles. The uniform-size microbubble-array artificial muscle exhibits no significant deformations in the absence of microbubbles. The sweeping frequency ranges from 1 to 100 kHz with a 60 V_{PP} input voltage, and the sweeping time per cycle is 10 seconds.

Movie S3. Characterization of variable-size microbubble-array artificial muscles.

(**I**) Static deformation under selectively constant frequency ultrasound actuation. The diameters of the microbubbles in the three different arrays, from top to bottom, are 12 μm, 16 μm, and 66 μm, with corresponding excitation frequencies of 96.5 kHz, 92.3 kHz, and 33.2 kHz. The input voltage is 60 V_{PP}. (**II**) Undulatory deformation under sweep-frequency ultrasound actuation. The variable-size microbubble-array artificial muscles undergoes undulatory motion as the frequency is swept from 30 to 100 kHz, covering all the natural frequencies of the three different radii microbubbles. Each cycle has a sweeping time of 1.2 seconds, and the input voltage is 60 V_{PP}.

Movie S4. Operation of microbubble-array soft grippers.

(**I**) Actuation of the soft grippers. The soft gripper is comprised of twelve uniform-sized artificial muscles, which are uniformly distributed in a manner resembling the petals of a flower. Each tentacle measures 10 mm, 0.7 mm, and 0.08 mm in length, width, and thickness, respectively, and houses 60,000 microbubbles when submerged in water. In the absence of ultrasound, the flower-shaped gripper remains at rest in an open state. When subjected to a continuous acoustic excitation at 95.5 kHz and 60 V_{PP}, it swiftly closes within 20 milliseconds; when the acoustic stimulus is deactivated, it reopens. (**II**) Operation at arbitrary locations. The gripper is held by a tweezer and is capable of functioning at random locations within the acoustic tank. The gripper operates with an input voltage of 60 V_{PP} and a frequency of 93.6 kHz. (**III**) Sweeping-frequency actuated grippers with different sizes microbubble-arrays. Three distinct grippers, each featuring tentacles

with microbubble-arrays in varying diameters: 12 μm, 16 μm, and 66 μm. These grippers can be sequentially activated by sweeping the frequency range from 30 to 100 kHz, with a sweeping duration of 1.2 seconds and an applied voltage of 60 V_{PP}.

Movie S5. Powering centimeter-scale bioinspired stingraybots.

(**I**) Swimming of the stingraybot. Each fin of the stingraybot is constructed using three microbubble-array artificial muscles with different diameters (40 μm, 60 μm, and 80 μm), arranged vertically from head to tail. The actuation is achieved by sweeping the frequency within the range of 30−90 kHz, with a sweep time of 1.8 seconds each cycle, and an input voltage of 60 V_{PP}. (**II**) Comparison between the stingraybot fin deformations with/without microbubbles. Excitation frequency: 60-100 kHz. Cycle duration: 1.5 seconds. Input voltage: 60 V_{PP}. Both experiments the stingray bot is fixed at the bottom.

Movie S6. Multi-modal deformation of the shape transformer.

Multi-mode shape transformation of a circular functional surface under the continuous ultrasound excitation frequencies of 96.2 kHz, 82.5 kHz, and 33.2 kHz, respectively.

Movie S7. Conformable robotic skin to impart motions to inanimate objects.

(**I**) Actuation of a piece of grass. Closing grass by a conformable microbubble-array robotic skin, where the excitation voltage and frequency are 60 V_{PP} and 96.2 kHz. (**II**) Actuation of the almond. Rotating of an almond by a conformable microbubble-array robotic skin, where the excitation voltage and frequency are 60 V_{PP} and 96.2 kHz.